Recent Geometric Flows in Multi-Orientation Image Processing via a Cartan Connection.

R. Duits, B.M.N. Smets, A.J. Wemmenhove, J.W. Portegies & E.J. Bekkers

Abstract Applications of geometric flows to multi-orientation image processing require the choice of an (affine) connection on the Lie group G of roto-translations. Typical choices of such connections are called the $(-)$, (0) and $(+)$ connection. As the constructions of these connections in standard references is quite involved, we provide an overview. We show that these connections are members of a larger, one-parameter class of connections, and we motivate that the $(+)$ connection is most suited for our image-analysis applications. The class $\nabla^{[\nu]}$, with $\nu \in \mathbb{R}$, is given by $\nabla^{[\nu]}_X Y = \nu\,[X,Y]$ for all left-invariant vector fields X,Y on G. Their auto-parallel curves are the exponential curves. Their torsion is $T[X,Y] = (2\nu - 1)[X,Y]$, and the $(-)$, (0), and $(+)$ connections arise for $\nu = 0, \frac{1}{2}, 1$.

We propose the case $\nu = 1$, as then the Hamiltonian flows on $T^*(G)$ for Riemannian distance minimizers on G (induced by left-invariant metric tensor field $\mathcal{G}$) reduce to $\nabla^{[1]}_{\dot{\gamma}}\lambda = 0$ and $\dot{\gamma} = \mathcal{G}|_{\gamma}^{-1}\,\lambda$, where $\dot{\gamma}$ is velocity and λ is momentum. So now 'shortest curves' have parallel momentum, whereas 'straight curves' have auto-parallel velocity. We also extend this idea to sub-Riemannian geometry via a partial connection.

The connection underlies PDE-flows for crossing-preserving geodesic wavefront propagation and denoising in multi-orientation image processing, where we use

1. the 'shortest curves' for tracking in multi-orientation image representations,
2. the 'straight curve fits' for locally adaptive frames in PDEs for crossing-preserving image denoising and enhancement.

Remco Duits, Bart Smets & Jelle Wemmenhove
ADG, Dep. of Mathematics and Computer Science, Eindhoven University of Technology, e-mail: R.Duits@tue.nl

Erik Bekkers
Amsterdam Machine Learning Lab, University of Amsterdam,

Jim Portegies
CASA, Dep. of Mathematics and Computer Science, Eindhoven University of Technology,

1 Introduction

The synergy between the mathematical fields of partial differential equations, geometric control, Lie group analysis, harmonic analysis, variational methods and the applied fields of image analysis, numerical analysis, neurogeometry and neuroimaging is increasing rapidly and has attracted many researchers. An emerging field for interaction between these fields is multi-orientation image analysis, where image data is lifted to the space of positions and orientations. Typically such lifted data is concentrated around lifted curves, see Figure 1.

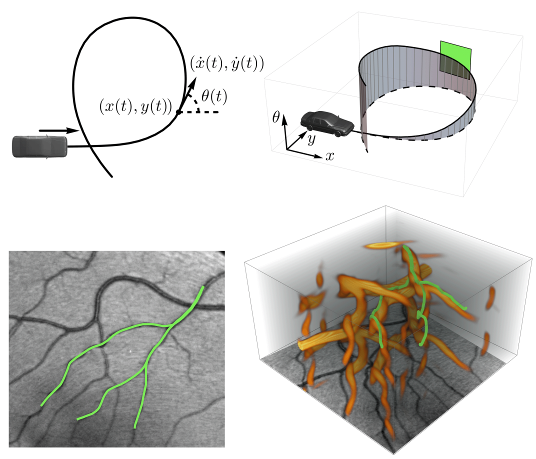

Fig. 1 Top: *Lifted paths* $\gamma(t) = (x(t), y(t), \theta(t))$ in $\mathbb{R}^2 \times S^1$ (left) where the tangent $\dot{\gamma}(t)$ is restricted to the span of $(\cos\theta(t), \sin\theta(t), 0)$ and $(0, 0, 1)$, of which the green plane on the right is an example. Bottom: *Lifted image data* depicted by an orange volume rendering. The meaning of shortest path between points in an image is determined by a combination of a cost computed from the lifted data, the restriction above, and a curvature penalization. The path optimization problem is formulated on the position-orientation domain such as in the image on the right. The cost for moving through the orange parts is lower than elsewhere.

There exist many ways to construct such orientation lifts of image data. For example, it can be done linearly by means of convolving the image by rotated and translated Gabor wavelets (where image reconstruction requires integration over scale and orientation) [1, 2], or by proper wavelets, including cake wavelets, (where inversion requires integration over angles only) [3, 4], or non-linearly via orientation channel representations [5, 6]. In the experiments of this article we constrain ourselves to invertible orientation scores [7] constructed by cake-wavelets following standard settings as explained in [4].

In multi-orientation processing on orientation scores [8, 3, 9, 10] (or on other orientation lifts [11, 1, 12, 13, 14]) differential geometry plays a fundamental role in PDE- and ODE-based techniques for pattern recognition, cortical modeling, and image analysis. Image processing applications are then provided with fundamental differential geometrical tools such as Cartan connections [15, 16] that 'literally connect' all tangent spaces in the tangent bundle $T(\mathbb{M}_d)$ above the space $\mathbb{M}_d$ of positions and orientations. Such a connection underlies flows [12], segmentations [17], detection [18], and tracking [19] on $\mathbb{M}_d$. In all of these PDE-based processing techniques on $\mathbb{M}_d$ one has the major benefit (over related algorithms acting directly in the image domain $\mathbb{R}^d$) that the processing generically deals with complex structures (such as crossings, bifurcations etc.). In this article we will highlight some applications in the experimental section, to illustrate how our preferred Cartan connection enters image analysis applications.

Here the key idea is that elongated structures that are involved in crossings, are manifestly disentangled in orientation lifts of image data, see Figure 2. This allows for crossing-preserving enhancements and tracking via such orientation lifts as shown in Figure 3. Furthermore, in the space of positions and orientations it is possible to

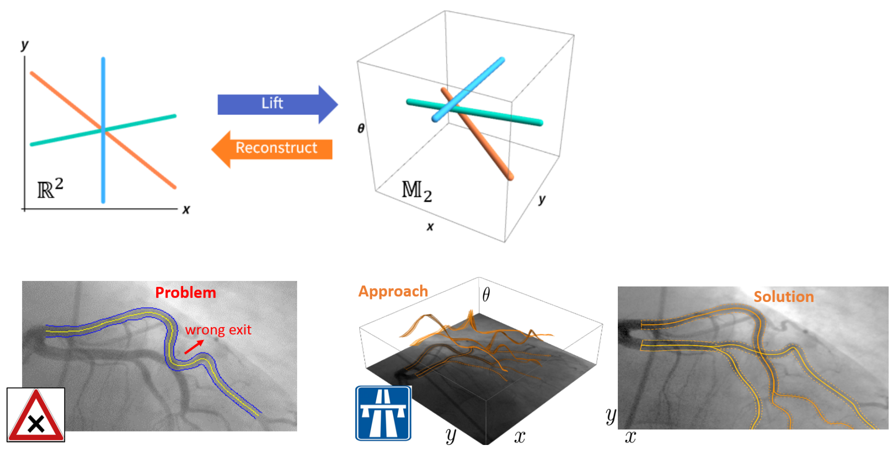

Fig. 2 Current tracking algorithms on images often fail (left), therefore we first extend the image domain to the space of positions and orientations (where no such crossings occur) and then apply geodesic tracking (right), enhancement and learning to automatically deal with complex structures.

check for alignment of local orientations in the image data. Filtering well-aligned local features in multi-orientation distributions (e.g. orientation scores) of image data is sometimes called 'contextual image processing' [20, 4, 21]. It relates to cortical models for line perception in human vision [22, 23, 1], and is highly beneficial for data enhancement and denoising in image analysis applications, see for example [10, 24, 13, 12, 14, 25, 26], prior to geometric tracking [27, 26, 28, 19] in the homogeneous space of positions and orientations.

The homogeneous space of positions is formally defined as a Lie group quotient

$$\mathbb{M}_d = G/H = SE(d)/(\{\mathbf{0}\} \times SO(d-1)) \tag{1}$$

in the Lie group $SE(d)$ of roto-translations on $\mathbb{R}^d$. We shall be concerned with applications of crossing-preserving denoising, analysis and tracking of line structures (blood vessels) via orientation scores, as depicted in Fig. 3. In the application section of this work, we mainly focus on the case $d = 2$, but we also highlight related works and applications where the case $d = 3$ is tackled.

Remark 1 The multi-orientation analysis of images is much simpler for $d = 2$ as then subgroup the H consists only of the unity element and thereby the Lie $SE(2)$ group of rotations and translations in the plane is isomorphic to the three dimensional homogeneous space $\mathbb{M}_2$ of positions and orientations. In case $d = 3$ the subgroup $H \equiv SO(2)$ and thereby the homogeneous space $\mathbb{M}_3$ of positions and orientations is five dimensional. In that case a multi-orientation distribution $U : \mathbb{M}_3 \to \mathbb{C}$ can be visualized by a field of angular profiles on a grid: $\{\mathbf{x} + \frac{|U(\mathbf{x},\mathbf{n})|}{2\|U\|_{\mathbb{L}_\infty(\mathbb{M}_3)}}\mathbf{n} \mid \mathbf{n} \in S^2, \mathbf{x} \in \mathbb{Z}^3\}$ with color coded orientations. For such a visualization see the bottom row of Fig. 3.

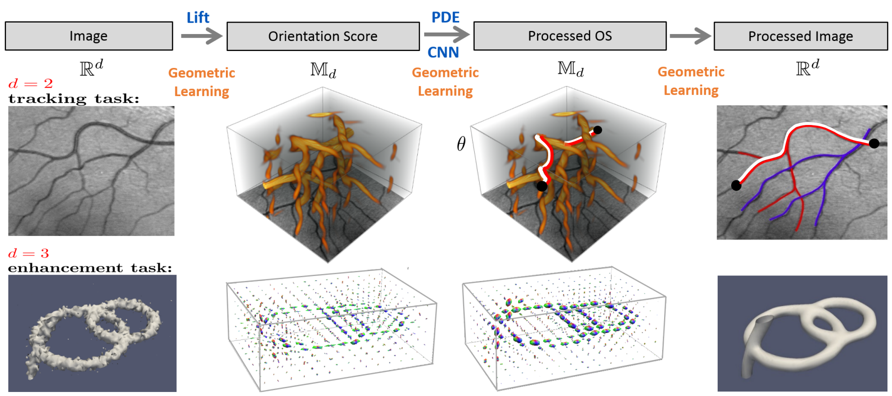

Fig. 3 Top: instead of direct processing of an image, we process via an invertible orientation score, obtained by convolving the image with a set of rotated wavelets [3, 4, 29]. 2nd row: vessel-tracking in a 2D image via orientation scores [4, 30, 19]. 3rd row: crossing-preserving diffusion via the orientation score of a 3D image [29, 31]. For automation one can integrate geometric deep learning via PDE-based G-CNNs [32] and G-CNNs [33, 34]. Here we will not elaborate on such machine learning techniques, but rather focus on the underlying PDEs and Cartan connection.

Remark 2 The idea of crossing-preserving denoising and tracking via multi-feature representations of images also generalizes to other 'scores' (multi-feature representations) on other Lie groups G (and Lie group quotients G/H):

- image processing of multi-frequency representations (Gabor transforms) [35] defined on the Heisenberg group $H(2d + 1)$,
- image processing of multi-velocity distributions (velocity scores) [36] defined on the Heisenberg group $H(2d + 1)$,

- image processing of spherical image data [37] defined on a quotient $S^2 \equiv SO(3)/SO(2)$ the rotation group $SO(3)$,
- image processing of multi-orientation and scale scores (continuous wavelet transforms) [38] on the similitude group $SIM(d)$.

In this article we shall not be concerned with applications of the other Lie group cases mentioned in the remark above, but in order to keep generality of our theoretical results we will initially study Cartan connections on Lie groups G in general, so that our results also apply to the general Lie group setting.

Furthermore, we deliberately avoid technical issues [39, 32, 40, 41] that come along with taking Lie group quotients like in (1). The differential geometrical results in this article are easier to grasp if one just considers the whole Lie group G. For integration of the appropriate symmetries that come along with taking Lie group quotients, with in particular the one of primary interest (1), see [39, 32, 40, 41].

1.1 Scores on Lie Groups $G = \mathbb{R}^d \rtimes T$ and the Motivation for left-invariant Processing and a left-invariant Connection on $T(G)$.

In the general Lie group setting we consider Lie groups $G = \mathbb{R}^d \rtimes T$ that are the semi-direct product of $\mathbb{R}^d$ with another Lie group T (reflecting the feature of interest, e.g. orientations, velocities, frequencies, scales etc.). Then one uses a unitary representation $g \mapsto \mathcal{U}_g$ of such a Lie group onto the space of images modeled by $\mathbb{L}_2(\mathbb{R}^d)$. to construct the 'score' (or 'lifted image') by probing image f by a family of group coherent wavelets constructed from a wavelet $\psi \in \mathbb{L}_2(\mathbb{R}^d) \cap \mathbb{L}_1(\mathbb{R}^d)$

$$\mathcal{W}_\psi f(g) = (\mathcal{U}_g\psi, f)_{\mathbb{L}_2(\mathbb{R}^d)}.$$

Clearly, not every (square integrable) function on the Lie-group is the orientation score of an image. It turns out that such a transform $\mathcal{W}_\psi : \mathbb{L}_2(\mathbb{R}^d) \to \mathbb{C}_K^G$ is a unitary map onto its range which is the unique reproducing kernel Hilbert space $\mathbb{C}_K^G$ consisting of functions on the Lie group G with reproducing kernel $K(g,h) = (\mathcal{U}_g\psi, \mathcal{U}_h\psi)_{\mathbb{L}_2(\mathbb{R}^d)}$. For details see [42, 43, 44].

Remark 3 In our special case of interest where the score is an 'orientation score', we set Lie group $G = SE(d) = \mathbb{R}^d \rtimes SO(d)$, for $d \in \{2,3\}$, with group product

$$g_1 g_2 = (\mathbf{x}_1, \mathbf{R}_1)(\mathbf{x}_2, \mathbf{R}_2) = (\mathbf{R}_1\mathbf{x}_2 + \mathbf{x}_1, \mathbf{R}_1\mathbf{R}_2), \qquad g_i = (\mathbf{x}_i, \mathbf{R}_i) \in SE(d), \tag{2}$$

for $i = 1,2$. Furthermore, we obtain the group coherent wavelets via the action

$$\mathcal{U}_g\psi(\mathbf{x}) = \psi(\mathbf{R}^{-1}(\mathbf{x} - \mathbf{b})), \tag{3}$$

for all $g = (\mathbf{b}, \mathbf{R}) \in SE(d)$, $\mathbf{x} \in \mathbb{R}^d$. In this case the family of group coherent wavelets are rotated and translated versions of ψ. For $d = 3$ one must assume that

ψ is rotationally symmetric around the reference axis in order to ensure that the orientation score $\mathcal{W}_\psi f$ is well-defined on $\mathbb{M}_3$. For details see [45].

The reproducing kernel norm coincides with a (constrained) $\mathbb{L}_2$-norm if $\mathcal{U}$ is irreducible [46]. This essentially follows by a generalization of Schur's lemma[1] [47].

Remark 4 If $\mathcal{U}$ is reducible, which is the case for the representation given by (3), one can apply a decomposition into irreducible subspaces [7, App.A]. Then one either must restrict the space of images (e.g. to the space of ball-limited images [44, ch.5.2],[42, ch.4.5]) or one must rely on distributional wavelet transforms [48, App.B]. In both cases one must take care that all coherently transformed wavelets $\mathcal{U}_g\psi$ together 'cover all the frequencies in the Fourier domain', see [42, 44, 49].

Let us define $\tilde{\mathcal{W}}_\psi : \mathbb{L}_2(\mathbb{R}^d) \to \mathbb{L}_2(G)$ by $\tilde{\mathcal{W}}_\psi f = \mathcal{W}_\psi f$. We can rely on the following commutative diagram to design operators in the enlarged image domain $G = \mathbb{R}^d \rtimes T$. As a consequence of the following Lemma, processing on scores must be left-invariant and not right-invariant.

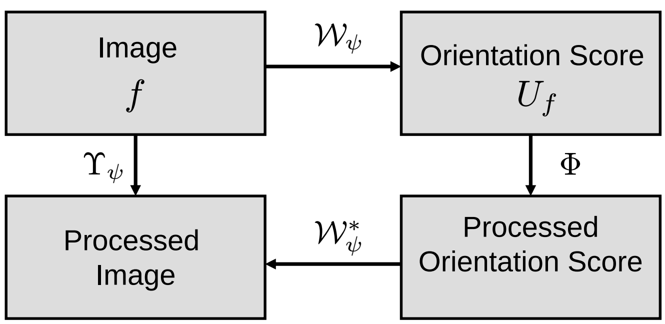

Fig. 4 A schematic view of image processing via scores. According to Lemma 1, Φ must be left-invariant and not right-invariant. The same applies to the other Lie group cases mentioned in Remark 2, where the score is not an 'orientation score' but for example a 'frequency score' [35].

Remark 5 In this article we will not address the issue of choosing a proper wavelet ψ. For the setting of $G = SE(3)$ or more precisely for $\mathbb{M}_3 = G/H$ we prefer to use so-called 'cake-wavelets' to construct invertible orientation scores [42]. For quick practical explanations on 2D cake-wavelets see [48], for the same on 3D cake-wavelets see [31]. All experiments in this chapter use cake-wavelets ψ with standard parameter settings [50]. For detailed educational background on invertible orientation scores, proper wavelets and cake-wavelets, see [49].

[1] The overall idea is that $\tilde{\mathcal{W}}_\psi^* \circ \tilde{\mathcal{W}}_\psi$ commutes with the unitary irreducible representation and is thereby a multiple of the identity. Subtleties arise as it is not obvious that $\tilde{\mathcal{W}}_\psi$ is bounded, cf. [46].

Definition 1 An operator $\Phi : \mathbb{L}_2(G) \to \mathbb{L}_2(G)$ is *left-invariant* iff

$$\Phi[\mathcal{L}_g V] = \mathcal{L}_g[\Phi V], \text{ for all } g \in G,\ V \in \mathbb{L}_2(G), \tag{4}$$

where the left-regular action $\mathcal{L}_g$ of $g \in G$ onto $\mathbb{L}_2(G)$ is given by

$$\mathcal{L}_g V(q) = V(g^{-1}q) \text{ for almost every } q \in G. \tag{5}$$

Similarly, the right-regular action is given by

$$\mathcal{R}_g V(q) = V(qg), \text{ for all } g, q \in G, V \in \mathbb{L}_2(G),$$

and an operator Φ is right-invariant $\Phi[\mathcal{R}_g V] = \mathcal{R}_g[\Phi V],$ for all $g \in G,\ V \in \mathbb{L}_2(G)$.

Lemma 1 *Let $\mathcal{U} : G \to B(\mathbb{L}_2(\mathbb{R}^d))$ be a unitary representation. Let $\Phi : \mathbb{C}_K^G \to \mathbb{L}_2(G)$ be a bounded operator. Then the corresponding operator Υ_ψ on $\mathbb{L}_2(\mathbb{R}^d)$ given by $\Upsilon_\psi[f] = (\tilde{\mathcal{W}}_\psi)^* \circ \Phi \circ \tilde{\mathcal{W}}_\psi[f]$ on the images $f \in \mathbb{L}_2(\mathbb{R}^d)$ satisfies*

$$\mathcal{U}_g \circ \Upsilon = \Upsilon \circ \mathcal{U}_g \textit{ for all } g \in G$$

if and only if the effective operator on the score $\mathbb{P}_\psi \circ \Phi$ is left-invariant, i.e.

$$\mathcal{L}_g(\mathbb{P}_\psi \circ \Phi) = (\mathbb{P}_\psi \circ \Phi)\mathcal{L}_g, \textit{ for all } g \in G,$$

which shows that score processing must be left-invariant. Moreover, we have

$$\Phi \circ \mathcal{R}_g = \mathcal{R}_g \circ \Phi \Rightarrow \Upsilon_\psi = \Upsilon_{\mathcal{U}_g \psi} \textit{ for all } g \in G,$$

which shows that right-invariance is a highly undesirable property for score processing.

See Figure 5 to get a visual impression what the above theorem means for the group of roto-translations in the plane $G = SE(2) \equiv \mathbb{M}_2$, recall Remark 3.

Proof This Lemma essentially gathers earlier results of the first author [42, Thm.21] and [35, Thm.1] where the proof can be found. □

Corollary 1 *We want to apply (second order) PDE-based operators Φ that involve covariant derivatives based on a connection. Both Φ and the connection should be left-invariant, and not right-invariant.*

In the sequel we will therefore study a specific family of left-invariant connections: A parameterized family ($\nu \in \mathbb{R}$) of Lie-Cartan connection, which, as we will see, contains one very special member: the case $\nu = 1$.

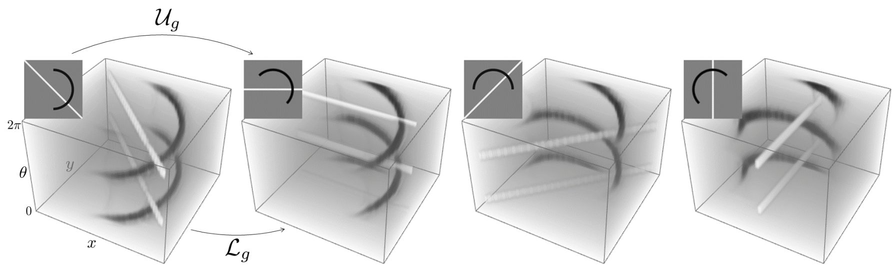

Fig. 5 A roto-translation of the image corresponds to a shift-twist of the orientation score, both defined via a group representations of $G = SE(2)$ on the image and the orientation score. Shift-twist of images and orientation scores are denoted respectively by the *left-regular* representations $\mathcal{U}_g$ (3) and $\mathcal{L}_g$ (5). In this illustration of $\mathcal{W}_\psi \circ \mathcal{U}_g = \mathcal{L}_g \circ \mathcal{W}_\psi$ we have set $g = (\mathbf{0}, \theta)$, with θ increasing from left to right.

1.2 Motivation: Choosing a Cartan Connection for Geometric (PDE-based) Image Processing via Scores

Geometric image processing via scores on Lie Groups requires a choice of underlying Cartan connection on $T(G)$. For geometric image processing we literally need to 'connect' tangent spaces $T_g(G)$ at different base-points $g \in G$ in the domain of a score. Such a connection gives rise to (coordinate free) covariant derivatives that we need in PDE-based image processing via scores on Lie groups. Next we will illustrate this on two geometric (PDE-based) image processing techniques:

1. Crossing-preserving image enhancement and denoising via scores, via geometric PDE's expressed in left-invariant/covariant derivatives.
2. Shortest paths (and optimal control) in orientation scores.

Crossing-preserving image enhancement and denoising via scores requires left-invariant PDE's and data-driven locally adaptive frames ('gauge frames') on G. The PDEs expressed in left-invariant frames include geometric flow along '*straight curves*' curves (with *parallel velocity*), which are exponential curves in Cartan connections. The PDEs expressed in gauge frames include geometric flow along 'straight curve fits' that solve a local curve optimization problem where straight-curve fits follow the data at each base-point $g \in G$ in a locally optimal way.

'*Shortest curves*' are paths that minimize a distance in G. We will show such shortest paths have *parallel momentum* with respect to a specific choice of Cartan connection. This will be the Lie-Cartan connection with $\nu = 1$.

The geometric notions of 'short' and 'straight' for curves will depend on the connection. Recall that such a connection must be left-invariant by Corollary 1, moreover it must account for torsion visible in the score (see Fig. 1).

1.3 Structure and Contributions of the Article

In this section we have so far provided an overview of geometric image processing via scores on Lie groups, with a particular focus on the case where the score is an orientation score defined on the homogeneous space of positions and orientations $\mathbb{M}_d$ as a Lie group quotient in $SE(d)$, recall (1). We also motivated the quest for choosing an effective Cartan connection as we need to 'connect' tangent spaces in PDE-flows for (crossing-preserving) enhancement and geodesic tracking in scores.

In Section 2 we will study a parameterized class (parameterized $\nu \in \mathbb{R}$) of Cartan connections, that we call 'Lie-Cartan' connections, that we will employ later on Riemannian geometry and Riemannian geometrical methods in later sections. We also consider partial Lie-Cartan connections to deal with the sub-Riemannian geometry setting. In *sub*-Riemannian geometry motions on $T(G)$ are constrained to a sub-bundle as other directions carry an 'infinite cost', this amounts to 'nonholonomic systems' in mechanics (cf. the green tangent plane restriction in Fig. 1).

In Section 3 we show that the Lie-Cartan connection with $\nu = 1$ is the best choice for geometric image processing on scores. We motivate this mainly with our new general result: Theorem 1. Roughly speaking, we show that shortest curves have parallel momentum as straight curves have parallel velocity.

In the remaining sections we drop the generality and focus on the case where the score is an orientation score defined on the homogeneous space $\mathbb{M}_d$ of positions and orientations, recall (1). We start in Section 4 to outline the details regarding this homogeneous space.

In Section 5 we study the shortest curves and the induced spheres on $\mathbb{M}_d$ where we put emphasis on the sub-Riemannian setting, with pointers to the literature.

In Section 6 we study the straight curves and data-driven straight curve fits in $SE(d)$ and their projections in $\mathbb{M}_d$.

Finally, in Section 7, we consider several image analysis applications. Three applications where the shortest curves in $\mathbb{M}_d$ play a central role, and four applications where the straight-curve fits in $\mathbb{M}_d$ play a central role:

- In Subsection 7.1 we use shortest curves (geodesics) in $\mathbb{M}_d$ to show that geodesic vessel tracking in $\mathbb{M}_d$ outperforms geodesic tracking in $\mathbb{R}^d$, and that sub-Riemannian geometric tracking outperforms isotropic Riemannian geometric tracking in $\mathbb{M}_d$. Initially we consider $d = 2$, but then in Subsection 7.1.1 we also address applications [19] for $d = 3$, and a new 3D vessel tracking experiment.
- In Subsection 7.2 we use straight curve fits in $\mathbb{M}_2 \equiv SE(2)$ for biomarkers of diabetes in retinal images.
- In Subsection 7.3 we use straight curve fits in $\mathbb{M}_2 \equiv SE(2)$ for image denoising. We also address extensions to $\mathbb{M}_3$:
  - In Subsection 7.3.1 we briefly highlight applications of the $\mathbb{M}_3$-case in enhancing fiber bundles in diffusion-weighted MRI (DW-MRI). For details see [51, 41].
  - In Subsection 7.3.2 we briefly highlight applications of the $\mathbb{M}_3$-case in denoising of 3D X-ray data. For details see [45].

Contributions: This article summarizes results and image analysis applications from previous works on PDE-based image processing via (orientation) scores [7, 30, 19, 52, 4, 35, 33, 41, 10], and more importantly, it puts them in a single novel geometrical perspective via a specific Lie-Cartan connection. Theorem 1 and Theorem 2 contain new general results. Lemma 2, Lemma 3 and Corollary 2 gather (standard) differential geometrical computations that are relevant in our quest of choosing an appropriate Cartan connection on Lie groups for geometric image processing via scores.

On the experimental side, we provide new experiments (e.g. Fig. 14), and illustrations (e.g. Fig. 18) and Tables (Tables 1,2), in addition to our previously published work. However, this is only with the intention of providing a general overview of the possibilities and impact of the differential geometric theory on many medical image analysis applications.

2 A Parameterized Class of Cartan Connections and their Duals

In this section we will address a parameterised class of Cartan connections on Lie groups that we will call 'Lie-Cartan' connections as they are induced by the Lie-bracket on the Lie group. We will adhere to references and conventions in the book by Kobayashi [53] and the recent review article by Cogliati [54].

Let G be a Lie group of dimension n. Let $\mathbb{L}_2(G)$ denote the space of square integrable functions on G endowed with the left-invariant Haar measure. Let $T_e(G)$ be the tangent space at unity element e. Let G be a Lie group such that the exponential map $\exp : T_e(G) \to G$ is surjective. Then $T_e(G)$ is a Lie Algebra with Lie-Bracket

$$\begin{aligned}[A,B] &= -\left.\tfrac{d}{dt}\right|_{t=0} (\gamma^{-B}(\sqrt{t})\; \gamma^{-A}(\sqrt{t})\; \gamma^{B}(\sqrt{t})\; \gamma^{A}(\sqrt{t})) \in T_e(G), \\ &= -\tfrac{1}{2}\left.\tfrac{d^2}{dt^2}\right|_{t=0} (\gamma^{-B}(t)\; \gamma^{-A}(t)\; \gamma^{B}(t)\; \gamma^{A}(t)),\end{aligned} \tag{6}$$

where $t \mapsto \gamma^X(t) = e^{tX}$ is a differentiable curve in G with $\gamma^X(0) = e$ and $(\gamma^X)'(0) = X$ for $X = A, B$. For details on Lie brackets see [55].
Let the right-regular representation $\mathcal{R} : G \to BL(\mathbb{L}_2(G))$ be given by $\mathcal{R}_g V(h) = V(hg)$. Then $\mathrm{d}\mathcal{R}$ is given by

$$(\mathrm{d}\mathcal{R}(A))V(g) = \lim_{t\downarrow 0} \frac{(\mathcal{R}_{e^{tA}} - I)V(g)}{t}, \text{ for } V \in \mathcal{D}(\mathrm{d}\mathcal{R}(A))$$

and the domain $\mathcal{D}(\mathrm{d}\mathcal{R}(A))$ of this unbounded operator $\mathcal{R}(A)$ is the subset of $\mathbb{L}_2(G)$ for which the above limit exists in $\mathbb{L}_2$-sense.

Let $L_g : G \to G$ denote the left-multiplication given by $L_g h = gh$. Let us choose a basis $\{A_1, \ldots, A_n\}$ in $T_e(G)$ and let us define the corresponding vector fields

$$\mathcal{A}_i|_g = (L_g)_* A_i, \text{ for } i = 1, \dots, n.$$

Let us define the corresponding dual basis ('left-invariant co-frame') in $T_g^*(G)$ by

$$\left\langle \omega^i\big|_g, \mathcal{A}_j\big|_g \right\rangle = \delta^i_j \tag{7}$$

with δ^i_j denoting the usual Kronecker delta. Then one has $\mathcal{A}_i = \mathrm{d}\mathcal{R}(A_i)$ and the structure constants c^k_{ij} of the Lie algebra relate via

$$[A_i, A_j] = \sum_{k=1}^{n} c^k_{ij} A_k \Leftrightarrow [\mathcal{A}_i, \mathcal{A}_j] = \mathcal{A}_i \circ \mathcal{A}_j - \mathcal{A}_j \circ \mathcal{A}_i = \sum_{k=1}^{n} c^k_{ij} \mathcal{A}_k. \tag{8}$$

If one imposes a left-invariant metric tensor field $g \mapsto \mathcal{G}_g(\cdot,\cdot) : T_g(G) \times T_g(G) \to \mathbb{R}$ to form a Riemannian manifold $(M, \mathcal{G})$ then there exists a unique *constant* matrix $[g_{ij}] \in \mathbb{R}^{n \times n}$ such that

$$\mathcal{G}_g = \sum_{i,j=1}^{n} g_{ij}\ \omega^i\big|_g \otimes \omega^j\big|_g .$$

for all $g \in G$. We restrict ourselves to the diagonal case

$$g_{ij} = \xi_i\ \delta_{ij} \tag{9}$$

with $\xi_i > 0$ for $i = 1, \dots, n$ and the Kronecker δ_{ij}. As a result for all $g \in G$ the mapping $(L_{g^{-1}})_* : T_g(G) \to T_e(G)$ is unitary. The mapping is known as the Cartan-Maurer form and 'connects' tangent spaces in a left-invariant way. See Fig. 6 where the Maurer-Cartan form is illustrated for the group $SE(2)$ of roto-translations in the plane with group product (2). The associated 'Cartan – connection' [53] is given by:

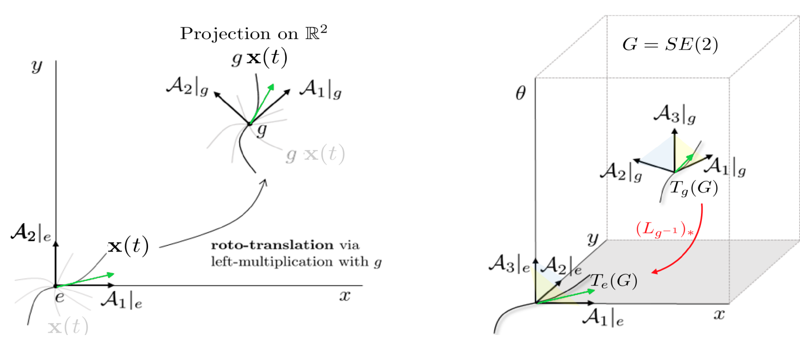

Fig. 6 The Maurer-Cartan form (in red) 'connects' tangent space $T_g(G)$ to $T_e(G)$ in a left-invariant way. It underlies the Lie-Cartan connection with $\nu = 0$ as can be seen in Lemma 2. Right we depict the Lie group case $SE(2) = \mathbb{R}^2 \rtimes S^1$ and left we show spatial projections $\mathbf{x}(t)$ of the curves $\gamma(t) = (\mathbf{x}(t), \theta(t)) \in SE(2)$.

$$\nabla^{-} := \sum_{i,k=1}^{n} \omega^{i} \otimes \left(\mathcal{A}_i \circ \omega^k(\cdot)\right) \mathcal{A}_k,$$

inducing a covariant derivative:

$$\nabla^{-}_{X} Y := \sum_{i,k=1}^{n} \omega^{i}(X) \left(\mathcal{A}_i(\omega^k(Y))\right) \mathcal{A}_k.$$

More precisely, for two arbitrary vector fields $X = \sum_{i=1}^{n} x^i \mathcal{A}_i$ and $Y = \sum_{j=1}^{n} y^j \mathcal{A}_j$, possibly non-left-invariant, (i.e. x^i and y^j need not be constant) one has

$$\nabla^{-}_{X} Y = \sum_{k=1}^{n} \left(\sum_{i=1}^{n} x^i \mathcal{A}_i y^k \right) \mathcal{A}_k.$$

This connection ∇^{-} has vanishing Christoffel symbols $\Gamma^k_{ij} = 0$ relative to the left-invariant frame (and co-frame) of reference, since

$$\Gamma^k_{ij} = \left\langle \omega^k, \nabla_{\mathcal{A}_i} \mathcal{A}_j \right\rangle. \tag{10}$$

This has big limitations and is not always the right choice for a connection on a Lie group G. Therefore, we consider a more general class of connections on the Lie group G, the so-called Lie-Cartan connections, as we define next. Then in particular we consider a 1-parameter class of Cartan connections. We will call these connections 'Lie-Cartan connections' as they are directly induced by the Lie-bracket.

Definition 2 Per [54, section 5.2], [56], a Cartan (or canonical) connection on a Lie group is a vector bundle connection with the following additional properties:

1. left invariance:

$$X, Y \text{ are left invariant vector fields} \Rightarrow \nabla_X Y \text{ is a left invariant vector field}, \tag{11}$$

2. for any $\mathbf{a} \in T_e(G)$ the exponential curve and auto-parallel curve coincide:

$$\nabla_{\dot{\gamma}(t)} \dot{\gamma}(t) = 0 \qquad \text{where} \qquad \gamma(t) = \gamma(0) \exp(t\mathbf{a}). \tag{12}$$

We now look at a specific set of Cartan connections that relate to the Lie bracket.

Definition 3 (Lie-Cartan Connection) Consider a Lie group with Lie brackets $[\cdot, \cdot]$ and structure constants $c^k_{ij} \in \mathbb{R}$ s.t. $\left[\mathcal{A}_i, \mathcal{A}_j\right] = \sum_k c^k_{ij} \mathcal{A}_k$. Then the Lie-Cartan connection indexed with $\nu \in \mathbb{R}$ equals:

$$\boxed{\nabla^{[\nu]} := \sum_{i,k=1}^{n} \omega^{i} \otimes \left(\mathcal{A}_i \circ \omega^k(\cdot)\right) \mathcal{A}_k + \sum_{i,j,k=1}^{n} \omega^i \otimes \omega^j \; \nu \, c^k_{ij} \; \mathcal{A}_k} \tag{13}$$

Remark 6 Left-invariant vector field X can be written as $X = \sum_{i=1}^{d} x^i \mathcal{A}_i$ with *constant* coefficients $x^i \in \mathbb{R}$. As a result we have that for left-invariant vector fields X, Y the first term vanishes in (13) and we have that $\nabla_X^{[\nu]} Y = \nu[X,Y]$.

Remark 7 The Christoffel symbols Γ_{ij}^k (10) relative to the left-invariant moving frame of reference equal $\Gamma_{ij}^k = \nu\, c_{ij}^k$ and vanish iff $\nu = 0$ and indeed one has for the classical 'minus' Cartan connection $\nabla^- = \nabla^{[0]}$. It is common [54, 53, 56, 57] to index the Cartan connections in terms of their Torsion $T_{\nabla^{[\nu]}}$ given by

$$T_{\nabla^{[\nu]}}(X,Y) := \nabla_X^{[\nu]} Y - \nabla_Y^{[\nu]} X - [X,Y] = (2\nu - 1)[X,Y],$$

for left-invariant vector fields X, Y, but we prefer to index the Lie-Cartan Connections $\nabla^{[\nu]}$ with the parameter ν arising in the commutator rather than with the parameter $2\nu - 1$ in the torsion of the connection:

$$\nabla^{[\nu]} = \nabla^{2\nu-1} \text{ and thus } \nabla^{[0]} = \nabla^-,\ \nabla^{[1]} = \nabla^+.$$

Remark 8 Lie-Cartan connections $\nabla^{[\nu]}$ are clearly connections on a vector bundle (satisfying the standard 4 requirements for Koszul connections).
Furthermore, they are indeed Cartan connections (Def. 2). The first item follows by Remark 6. The second item follows by anti-symmetry of the Christoffel symbols relative to the left-invariant frame of vector fields. We will show this later in (41).

Lemma 2 *For arbitrary smooth vector fields X,Y on G we have*

$$(\nabla_{\dot{\gamma}}^{[0]} Y)(g) = \lim_{t \to 0} \frac{\left(L_{g(\gamma(t))^{-1}}\right)_* Y(\gamma(t)) - Y(g)}{t}. \tag{14}$$

For left-invariant vector fields X,Y on G, we have

$$\begin{aligned} \nu = 0 : \quad & \nabla^{[0]} Y &&= 0\,, \\ \nu \in \mathbb{R} : (& \nabla_{\dot{\gamma}}^{[\nu]} Y)(g) &&= \lim_{t \to 0} \tfrac{(\widetilde{Ad}(\gamma(\nu t))Y)(g) - Y(g)}{t} \text{ i.e.} \\ & \nabla_X^{[\nu]} Y &&= \nu[X,Y]\,, \end{aligned} \tag{15}$$

with $\gamma(t)$ is an integral curve of left-invariant vector field X with $\gamma(0) = g \in G$, and

$$\widetilde{Ad}(q) = (L_g)_* \circ Ad(q) \circ (L_{g^{-1}})_*, \tag{16}$$

with $Ad(g) = (L_g \circ R_{g^{-1}})_* : T_e(G) \to T_e(G)$, where $(\cdot)_*$ denotes the push-forward, so that $(Ad)_* = ad$ with $ad(X_e)(Y_e) = [X_e, Y_e]$, and the transferred adjoint representation given by $\widetilde{Ad}(g) = (L_g \circ R_{g^{-1}})_* : T_g(G) \to T_g(G)$ that satisfies

$$(\widetilde{Ad})_*(X_g)(Y_g) = [X_g, Y_g] \text{ for all } g \in G. \tag{17}$$

Proof The proof follows by direct computations, see Appendix C. □

Lemma 3 *(Properties of the Lie-Cartan connections)*
Let X, Y, Z be left-invariant vector fields.
The torsion tensor gives

$$T_{\nabla^{[\nu]}}(X,Y) = (2\nu - 1)[X,Y]. \tag{18}$$

The curvature tensor gives

$$R_{\nabla^{[\nu]}}(X,Y)Z = \nu(1-\nu)[Z,[X,Y]]. \tag{19}$$

Relative to the left-invariant frame on G we have the following components:
$T^i_{jk} = (2\nu - 1)c^i_{jk}$ *and* $R^l_{k,ij} = \nu(1-\nu)\sum\limits_{q=1}^{n} c^l_{kq} c^q_{ij}$.
The Lie-Cartan connections satisfy the following identity:

$$(\nabla^{[\nu]}\mathcal{G})(X,Y,Z) = -\nu\left(\mathcal{G}([X,Y],Z) + \mathcal{G}([X,Z],Y)\right). \tag{20}$$

Proof The proof can be found in Appendix C. □

Remark 9 (from left-invariant vector fields to general vector fields)
The formulas above in Lemma 3 only hold for left-invariant vector fields. For example, the general formula for the torsion is

$$T_{\nabla^{[\nu]}} = (2\nu - 1)\sum_{i,j,k=1}^{n} \omega^i \otimes \omega^j \, c^k_{ij}\, \mathcal{A}_k. \tag{21}$$

so only for left-invariant vector fields do we have $T_{\nabla^{[\nu]}}(X,Y) = (2\nu-1)[X,Y]$. It is not a coincidence that vanishing torsion for arbitrary non-commuting vector fields gives $\nu = \frac{1}{2}$, whereas the same conclusion can be drawn from left-invariant non-commuting vector fields. In general, the torsion T_∇ and curvature R_∇ of a connection, and the covariant derivative $\nabla\mathcal{G}$ of the metric tensor fields, are *tensor fields*, so e.g.

$$\begin{aligned}&T_{\nabla^{[\nu]}}(f_1X_1 + f_2X_2, g_1Y_1 + g_2Y_2) = \\ &f_1g_1T_{\nabla^{[\nu]}}(X_1,Y_1) + f_2g_1T_{\nabla^{[\nu]}}(X_2,Y_1) + f_1g_2T_{\nabla^{[\nu]}}(X_1,Y_2) + f_2g_2T_{\nabla^{[\nu]}}(X_2,Y_2)\end{aligned} \tag{22}$$

for all $f_i, g_i \in C^\infty(G)$ and all vector fields X_i, Y_i on G, $i = 1,2$.

Corollary 2 *Let G be a non-commutative Lie group and assume G is not 2-step nilpotent. The Lie-Cartan connection $\nabla^{[\nu]}$ is*

1. *torsion free iff $\nu = \frac{1}{2}$,*
2. *curvature free iff $\nu \in \{0,1\}$*
3. *metric compatible w.r.t. left-invariant metric $\mathcal{G}$ if $\nu = 0$.*

Proof By Remark 9 we may as well restrict our Lie-Cartan connection $\nabla^{[\nu]}$ to left-invariant vector fields, since T_∇, R_∇ and $\nabla\mathcal{G}$ are all tensor fields. Therefore they have

C^∞- linearity (such as in (22)) in all of their entries. This C^∞ linearity allows us to turn arbitrary vector fields into left-invariant vector fields by linear combinations.

The first item now follows by (18) and G being non-commutative (i.e. there exist left-invariant vector fields X, Y s.t. $[X,Y] \neq 0$ as $2\nu - 1 = 0 \Leftrightarrow \nu = \frac{1}{2}$). Note that it also follows by (21). The second item follows by (19) and by the assumptions on G there exist (left-invariant) X, Y, Z s.t. $[Z,[X,Y]] \neq 0$, and thereby $\nu(1-\nu) \Leftrightarrow \nu \in \{0,1\}$. The third item follows by (20) as for metric compatibility the covariant derivative of the metric tensor should vanish. □

The above properties explain why the choices $\nu \in \{0, \frac{1}{2}, 1\}$ are the most common choices for Cartan connections. Our application (recall Fig. 1) will require torsion and metric-incompatibility of connections on G. Metric incompatibility allows us to distinguish between 'straight curves' (auto-parallel curves with parallel velocity) and 'shortest curves' (distance minimizing geodesics with parallel momentum), as we will see in Theorem 1.

2.1 Expressing the Lie-Cartan connection (and its Dual) in Left-invariant Coordinates

Now that we defined the Lie-Cartan connections and that we addressed their fundamental geometric properties, we express them explicitly in left-invariant coordinates.

The covariant derivative of a field $Y = \sum_{k=1}^{n} y^k \mathcal{A}_k$, along a smooth vector field $X = \sum_{i=1}^{n} x^i \mathcal{A}_i$ is given by (for details see Remark 10 below)

$$\nabla_X^{[\nu]} Y = \sum_{k=1}^{n} \left(\dot{y}^k + \sum_{i,j=1}^{n} \nu c_{ij}^k x^i y^j \right) \mathcal{A}_k. \tag{23}$$

where we use common short notation [58, (3.1.6)] $\dot{y}^k(t) = \frac{d}{dt} y^k(\gamma(t))$ which equals $\dot{y}^k(t) = (X y^k)(\gamma(t))$ and $x^i = \dot{\gamma}^i(t)$ where $x^i\big|_{\gamma(t)} := \gamma^i(t) = \langle \omega^i\big|_{\gamma(t)}, \dot{\gamma}(t)\rangle$ along all flow-lines γ of smooth vector field X. A 'flowline' is a smooth curve γ satisfying $\dot{\gamma}(t) = X_{\gamma(t)})$. With slight abuse of notation we write

$$\nabla_{\dot{\gamma}}^{[\nu]} Y = \sum_{k=1}^{n} \left(\dot{y}^k + \sum_{i,j=1}^{n} \nu\, c_{ij}^k \dot{\gamma}^i y^j \right) \mathcal{A}_k. \tag{24}$$

The corresponding dual connection on the co-tangent bundle is given by

$$\nabla_{\dot{\gamma}}^{[\nu],*} \lambda = \sum_{i=1}^{n} \left(\dot{\lambda}_i + \sum_{k,j=1}^{n} \nu\, c_{ij}^k \lambda_k \dot{\gamma}^j \right) \omega^i, \tag{25}$$

where $\lambda = \sum_{i=1}^{n} \lambda_i \, \omega^i \in T^*(G)$. Note that $\langle \nabla^{[\nu],*}_X \lambda, Y\rangle = X\langle \lambda, Y\rangle - \langle \lambda, \nabla^{[\nu]}_X Y\rangle$ and from this formula we see how (25) follows from (24). The fact that both formulas involve a plus sign for the summation reflects that the Christoffel symbols [58] of the connection and dual connection (in the left-invariant frame) are each others inverse:

$$0 = \nu(c^k_{ji} + c^k_{ij}) = \langle \nabla^{[\nu],*}_{\mathcal{A}_i} \omega^k, \mathcal{A}_j\rangle + \langle \omega^k, \nabla^{[\nu]}_{\mathcal{A}_i} \mathcal{A}_j\rangle.$$

Remark 10 Next we explain how (23) follows by the corresponding (previously addressed) coordinate free formulation (13):

$$\begin{aligned}
\nabla^{[\nu]}_X(Y) := \nabla^{[\nu]}(X,Y) &= \sum_{i,j,k=1}^{n} \left(\left(\omega^i \otimes \left(\mathcal{A}_i \circ \omega^k(\cdot)\right)\right)(X,Y) + \omega^i(X)\, \omega^j(Y)\, \nu c^k_{ij} \right) \mathcal{A}_k \\
&= \sum_{i,k=1}^{n} x^i \, (\mathcal{A}_i y^k) \mathcal{A}_k + \sum_{i,j,k=1}^{n} \nu c^k_{ij} x^i y^j \, \mathcal{A}_k,
\end{aligned}$$

with $X|_\gamma = \sum_{i=1}^{n} x^i \; \mathcal{A}_i|_{\gamma(\cdot)} = \dot{\gamma} = \sum_{i=1}^{n} \dot{\gamma}^i \; \mathcal{A}_i|_{\gamma(\cdot)}$ and $Y = \sum_{k=1}^{n} y^k \mathcal{A}_k$, and
$\dot{y}^k(t) = \frac{d}{dt} y^k(\gamma(t)) = \sum_{i=1}^{n} x^i \, (\mathcal{A}_i y^k)(\gamma(t)) = X(y^k)(\gamma(t))$ via the chain-law.

2.2 (Partial) Lie-Cartan connections for (Sub)-Riemannian Geometry

The Lie-Cartan connections introduced will be in support of understanding Riemannian geometry when the Lie group is considered as a Riemannian manifold $(G, \mathcal{G})$ with a left-invariant Riemannian metric tensor field given by

$$\mathcal{G} = \sum_{i,j=1}^{n} g_{ij} \; \omega^i \otimes \omega^j, \tag{26}$$

with g_{ij} constant relative to the left-invariant co-frame ω^i given by (7) s.t. matrix $[g_{ij}] \in \mathbb{R}^{n \times n}$ is symmetric positive definite. Recall we restricted ourselves to the diagonal case (9). The linear map associated to metric tensor field $\mathcal{G}$ is written as

$$\tilde{\mathcal{G}}(X) = \mathcal{G}(X, \cdot) \tag{27}$$

In many applications (robotics [59, 60], image analysis [30], cortical vision [61, 22]) it is useful to rely on sub-Riemannian geometry [62] where certain direction in the tangent bundle are forbidden as they go with infinite cost. This means that tangents of connecting curves are prescribed to be in a sub-bundle Δ (also known as 'distribution') of the tangent bundle $T(G)$, i.e.

$$\dot{\gamma}(t) \in \Delta_{\gamma(t)} \subset T_{\gamma(t)}(G) \text{ for all } t \in \mathrm{Dom}(\gamma) \subset \mathbb{R}.$$

Typically for a controllable system, Δ and its commutators should fill the full tangent space, in view of Hörmander's theorem [63]. Here we will constrain ourselves to the case that the Lie-algebra is 2-bracket generating:

$$\Delta + [\Delta, \Delta] = T(G). \tag{28}$$

Remark 11 For instance, let us consider the car in Fig. 1 that needs to move in Lie group $SE(2)$. As the car can proceed forward (by giving gas) and change its orientation (by turning the wheel), it cannot move sidewards. Optimal paths for the car boil down to sub-Riemannian geodesic problems in which the partial Cartan connection $\overline{\nabla}^{[1]}$ will play a major role, as we will show in the next subsection.

Now let us assume that we label the Lie algebra in such a way that

$$\Delta = \mathrm{Span}\{\mathcal{A}_i\}_{i \in I} \tag{29}$$

for some index set $I \subset \{1, \ldots, n\}$ and recall that we assumed (28) to hold.

This allows us to consider *partial Cartan connections* on G that will play a major role on sub-Riemannian problems on sub-Riemannian manifolds $(G, \Delta, \mathcal{G}_0)$ with

$$\mathcal{G}_0 = \sum_{i,j \in I} g_{ij}\ \omega^i \otimes \omega^j, \tag{30}$$

as we will see later. Again we restrict ourselves to the diagonal case $g_{ij} = \xi_i \delta_{ij}$.

Definition 4 (Partial Lie-Cartan Connection)

Consider a Lie group with Lie brackets $[\cdot, \cdot]$ and structure constants $c^k_{ij} \in \mathbb{R}$ so that

$$\left[\mathcal{A}_i, \mathcal{A}_j\right] = \sum_{k=1}^{n} c^k_{ij} \mathcal{A}_k.$$

Consider the distribution given by (29). Then the partial Lie-Cartan connection with parameter $\nu \in \mathbb{R}$ (defined only on vector fields that map into the distribution) equals:

$$\boxed{\overline{\nabla}^{[\nu]} := \sum_{i,k \in I} \omega^i \otimes \left(\mathcal{A}_i \circ \omega^k(\cdot)\right)\ \mathcal{A}_k + \sum_{i,j,k \in I} \omega^i \otimes \omega^j\ \nu c^k_{ij}\ \mathcal{A}_k,} \tag{31}$$

So from this definition we deduce that

$$\begin{aligned} \overline{\nabla}^{[\nu]}_{\dot{\gamma}} Y &= \sum_{i,j,k \in I} \left(\dot{y}^k + \nu c^k_{ij} \dot{\gamma}^i y^j\right)\ \mathcal{A}_k\ , \\ \overline{\nabla}^{[\nu],*}_{X} \lambda &= \sum_{i=1}^{n} \left(\dot{\lambda}_i + \nu \sum_{k=1}^{n} \sum_{j \in I} c^k_{ij} \lambda_k \dot{\gamma}^j\right) \omega^i, \end{aligned} \tag{32}$$

where we highlighted the difference with the full Lie-Cartan connection in red, compare to Def 3, (24), (25). Again X, Y are vector fields and λ a dual vector field and γ is an integral curve of X, and $\dot{y}^k(t) := \frac{d}{dt} y^k(\gamma(t))$, $\dot{\lambda}_k(t) := \frac{d}{dt} \lambda_k(\gamma(t))$.

3 The Special Case of Interest $\nu = 1$ and Hamiltonian Flows for the Riemannian Geodesic Problem on G

Let $C : G \to \mathbb{R}^+$ be an a priori smooth cost (or mobility) for moving through q Lie group G that is bounded from below. For the moment it can be considered as constant, but later on in the application sections it will play an important role.

Then the Riemannian metric tensor field $\mathcal{G}$ induces a Riemannian metric on G:

$$d_{\mathcal{G}}(g_0, g_1) := \min_{\substack{\gamma \in \text{Lip}([0,1],G) \\ \gamma(0)=g_0, \\ \gamma(1)=g_1,}} \int_0^1 C(\gamma(t)) \sqrt{\mathcal{G}|_{\gamma(t)}(\dot{\gamma}(t), \dot{\gamma}(t))}\, \mathrm{d}t. \tag{33}$$

for all $g_0, g_1 \in G$. The sub-Riemannian metric tensor field $\mathcal{G}_0$ induces a sub-Riemannian metric on G by $d_{\mathcal{G}_0} : G \times G \to \mathbb{R}^+$ on G:

$$d_{\mathcal{G}_0}(g_0, g_1) := \min_{\substack{\gamma \in \text{Lip}([0,1],G) \\ \gamma(0)=g_0, \\ \gamma(1)=g_1, \\ \forall_{t\in[0,1]} \,:\, \dot{\gamma}(t) \in \Delta|_{\gamma(t)}}} \int_0^1 C(\gamma(t)) \sqrt{\mathcal{G}_0|_{\gamma(t)}(\dot{\gamma}(t), \dot{\gamma}(t))}\, \mathrm{d}t. \tag{34}$$

for all $g_0, g_1 \in G$. The next theorem motivates the choice $\nu = 1$ for the Lie-Cartan connection $\nabla^{[1]}$, that is underlying the Hamiltonian flow associated to (33).

Recall from geometric control theory [62, 64] that the Pontryagin Maximum Principle describes the Hamiltonian flow. It allows us to simultaneously analyze all lifted geodesics $(\gamma(\cdot), \lambda(\cdot))$ in the co-tangent bundle $T^*(G)$, where $\lambda(\cdot)$ denotes the momentum along the geodesic. This is important, as a single (analytic) description of a geodesic typically does not say that much. It is rather the continuum of geodesics and how their lifted versions in $T^*(G)$ are organized that help us understanding their behavior. This is well-known for classical problems like the 'mathematical pendulum', but it is also crucial in understanding the cut-locus [65] of the 'sub-Riemannian geodesic' problem or the 'elastica problem' [66, 67, 68] in $SE(2)$ as shown by Sachkov. For cortical contour perception models [69, 1], this is equally important.

However, the underlying deep role of Cartan connections is often not mentioned, despite its use in deriving simple solutions to cusp-free sub-Riemannian geodesics in $SE(2)$ solving association field models [16], and for new solutions [70] of sub-Riemannian geodesics in $SE(3)$. The power of such Cartan connections is also stressed in the Lagrangian geometric viewpoint on optimal curves by Bryant [71, 67].

In this work we take the venture point of the geometric Hamiltonian viewpoint on (sub-)Riemannian geometry [64, 62] and include a key element coming from Bryant's Lagrangian viewpoint on contact manifolds (and his analysis of 'elastica' [67]): That is (partial) Cartan connections that carry torsion. They will allow us to distinguish between 'shortest' and 'straight' curves in Lie groups. For multi-orientation image processing this is very useful and intuitive as we show in Thm. 1, Fig. 7 and Section 7.

Theorem 1 *In a Riemannian manifold $(G, T(G), \mathcal{G})$, with the tangent bundle $T(G)$ and metric tensor field $\mathcal{G}$ defined in (26) and the induced metric $d_{\mathcal{G}}$ defined in (33), and the Lie-Cartan connection $\nabla^{[\nu]}$ for $\nu = 1$ defined in (13), we have the following relations for "straight" curves:*

$$\begin{array}{ccccc} & \gamma \textit{ is a } \nabla^{[1]}\textit{-straight curve} & \Leftrightarrow & \gamma \textit{ is an exponential curve} & \\ \Leftrightarrow & \nabla^{[1]}_{\dot{\gamma}}\dot{\gamma} = 0 & \Leftrightarrow & \gamma \textit{ has } \nabla^{[1]}\textit{-auto parallel velocity} & , \end{array} \tag{35}$$

and the following for "shortest" curves (minimizers in (33)), recall also (27):

$$\begin{array}{ccc} \gamma \textit{ is a shortest curve} & \Leftrightarrow & \gamma \textit{ is a minimizing curve in } d_{\mathcal{G}} \\ \Rightarrow \begin{cases} \nabla^{[1],*}_{\dot{\gamma}}\lambda = 0 \\ \dot{\gamma} = \tilde{\mathcal{G}}^{-1}\lambda \end{cases} & \Leftrightarrow & \gamma \textit{ has } \nabla^{[1],*}\textit{-parallel momentum} \quad . \end{array} \tag{36}$$

In a sub-Riemannian (SR) manifold $(SE(2), \Delta, \mathcal{G}_0)$ with sub-bundle Δ defined in (31), the sub-Riemannian metric tensor $\mathcal{G}_0$ (30) and distance (34), and partial Cartan connection (31), we have the following relations for "straight" curves:

$$\begin{array}{ccc} \gamma \textit{ is a } \overline{\nabla}^{[1]}\textit{-straight curve} & \Leftrightarrow & \gamma \textit{ is a horizontal exponential curve} \\ \Leftrightarrow \quad \overline{\nabla}^{[1]}_{\dot{\gamma}}\dot{\gamma} = 0 & \Leftrightarrow & \gamma \textit{ has } \overline{\nabla}^{[1]}\textit{-auto parallel velocity} \; , \end{array} \tag{37}$$

and the following for "shortest" curves (minimizers in (34)):

$$\begin{array}{ccc} \gamma_0 \textit{ is a shortest curve} & \Leftrightarrow & \gamma_0 \textit{ is a minimizing curve in } d_{\mathcal{G}_0} \\ \Rightarrow \begin{cases} \overline{\nabla}^{[1],*}_{\dot{\gamma}_0}\lambda = 0 \\ \dot{\gamma}_0 = \tilde{\mathcal{G}}_0^{-1}\mathbb{P}^*_\Delta\lambda \end{cases} & \Leftrightarrow & \gamma_0 \textit{ has } \overline{\nabla}^{[1],*}\textit{-parallel momentum} \; , \end{array} \tag{38}$$

in which $\mathbb{P}^*_\Delta$ is the projection $\mathbb{P}^*_\Delta\left(\sum_{i=1}^n \lambda_i\omega^i\right) = \sum_{i\in I}\lambda_i\omega^i$. For the reverse in (36) and (38); for a minimizing curve between $g_1 = \gamma(0)$ and $g_2 = \gamma(t)$ one must have $0 \leq t \leq t_{cut} = \min\{t_{conj}(\lambda(0)), t_{Max,1}(\lambda(0)\}$, cf. [62, 65] for details.
The shortest curve $\gamma : [0,1] \to G$ with $\gamma(0) = g$ and $\gamma(1) = g_0$ may be computed by steepest descent backtracking on the distance map $W(g) = d_{\mathcal{G}^U}(g, g_0)$

$$\gamma(t) := \gamma^U_{g,g_0}(t) = Exp_g(t\; \overrightarrow{\mathfrak{h}^1(W)}) \qquad t \in [0,1], \tag{39}$$

where Exp integrates the vector field $\overrightarrow{\mathfrak{h}^1(W)} := -W(g)\, grad_{\mathcal{G}}W(g) = -W(g) \sum_{k=1}^n g^{kk}\mathcal{A}_k(W)\mathcal{A}_k$ on G and where W is the unique viscosity solution of the eikonal PDE system:

$$\begin{cases} \|grad_{\mathcal{G}}W(g)\| = \sqrt{\mathcal{G}|_g\,(grad_{\mathcal{G}}W(g), grad_{\mathcal{G}}W(g))} = 1, \\ W(e) = 0. \end{cases} \tag{40}$$

Proof First we address the 'shortest curves' part of the theorem. The items (36) and (38) follow by the Pontryagin Maximum Principle [62] and Theorem 2 in Appendix A. Theorem 2 proves the actual fundamental relation between the (partial) Lie-Cartan connection $\nabla^{[1]}$ to the Hamiltonian flow, for the (sub)-Riemannian setting. Here we stress that PMP provides only *local* optimality of geodesics.

The geodesics are found by the exponential map that integrates the Hamiltonian flow $(\lambda(0), t) \mapsto (\gamma(t), \lambda(t)) = e^{t\mathfrak{h}}(\lambda_0)$.

Optimality of $t \mapsto \gamma(t)$, requires t to be less than the cut-time. Such a cut-time is the minimum of the conjugate time $t_{conj}(\lambda(0)) \in \mathbb{R} \cup \{\infty\}$ where local optimality is lost, and the first Maxwell time $t_{Max,1}$, where two equidistant geodesics meet for the first time and where global optimality is lost. Now $t \leq t_{cut}(\lambda(0))$ is guaranteed by steepest descent (39) on the distance maps W which are obtained as viscosity solutions [72, 73] to the eikonal PDE. This is well-known for the Riemannian case [74, 72], but also applies to the sub-Riemannian[2] case [75, 30] and holds even in more general Finsler geometrical settings [19].

Secondly, regarding the 'straight curves' (35) one has (by (24)) and anti-symmetry of the structure constants (8) that:

$$
\begin{aligned}
\nabla^{[1]}_{\dot{\gamma}}\dot{\gamma} = 0 &\Leftrightarrow \forall_{k \in \{1,\ldots,n\}} \ : \ \ddot{\gamma}^k - \sum_{i,j=1}^{n} c^k_{ij}\dot{\gamma}^i\dot{\gamma}^j = \ddot{\gamma}^k = 0 \\
&\Leftrightarrow \forall_{k \in \{1,\ldots,n\}} \ : \ \langle \omega^k \big|_{\gamma}, \dot{\gamma}\rangle =: \dot{\gamma}^k = c^k = \text{ constant} \\
&\Leftrightarrow \gamma(t) = \gamma(0)\, e^{t\sum_{k=1}^{n} c^k A_k},
\end{aligned}
\tag{41}
$$

with $\ddot{\gamma}^k(t) = \frac{d}{dt}\dot{\gamma}^k(t)$. Note that the first, third and fourth statement in (35) are just tautological, so that (41) proves the remaining second equivalence. The SR-case (37) follows similarly by (32) taking into account the restriction to (29) via projection P^*_{Δ} which means we constrain the summations to index set I and set $\dot{\gamma}^i = 0$ if $i \notin I$. □

For 2D image processing via orientation scores [7, 76, 4, 77] we must consider the special case:

$$
\boxed{
\begin{array}{ll}
G & = SE(2), \\
\mathcal{A}_1 & = \cos\theta\partial_x + \sin\theta\partial_y,\ \mathcal{A}_2 = -\sin\theta\partial_x + \cos\theta\partial_y,\ \mathcal{A}_3 = \partial_\theta, \\
I = \{1,3\} & \Rightarrow \Delta = \text{span}\{\mathcal{A}_1, \mathcal{A}_3\}, \\
\mathcal{G}_0 & = \xi^2\omega^1 \otimes \omega^1 + \omega^3 \otimes \omega^3 \\
 & = \xi^2(\cos\theta \mathrm{d}x + \sin\theta \mathrm{d}y) \otimes (\cos\theta \mathrm{d}x + \sin\theta \mathrm{d}y) + \mathrm{d}\theta \otimes \mathrm{d}\theta, \\
\mathcal{G} & = \mathcal{G}_0 + \xi^2\zeta^{-2}(-\sin\theta \mathrm{d}x + \cos\theta \mathrm{d}y) \otimes (-\sin\theta \mathrm{d}x + \cos\theta \mathrm{d}y),
\end{array}
}
\tag{42}
$$

with curve stiffness parameter $\xi > 0$ and with anisotropy parameter $0 < \zeta \ll 1$. The basic idea here is that one considers a path optimization via a Reeds-Shepp car moving in the orientation score ($\xi > 0$ puts relative costs on moving forward

---

[2] For an intuitive illustration on inside the viscosity solutions of the PDEs non-optimal wavefronts are cut (at the 1st Maxwell set) in the sub-Riemannian setting (42), see [30, Fig.3].

to turning the wheel of the car), see Figure 1. In Figure 1 the green plane indicates $\Delta_g \subset T_g(G)$ for some $g = (x, y, \theta) \in SE(2)$. This 2D subspace is the subspace to which local velocities are constrained in the sub-Riemannian setting, i.e. $\dot{\gamma}(0) \in \Delta_g$ for all smooth 'horizontal' curves γ in the sub-Riemannian manifold with $\gamma(0) = g$.

The geometric control problem (34) is then concerned with finding the shortest path for the car in the orientation score. See Figure 7 for an intuitive illustration of Theorem 1 in the $SE(2)$-setting (42). In order to generalize this special case from $d = 2$ to $d = 3$ we must distinguish between the homogeneous space $\mathbb{R}^d \rtimes S^{d-1}$ of positions and orientations on which the rigid body motion group $SE(d)$ acts, and the Lie group itself. This will be the topic of the next section.

4 The Homogeneous Space $\mathbb{M}_d$ of Positions and Orientations

We consider geometric image processing on the homogeneous space of positions and orientations which equals the partition of left-cosets given by:

$$\mathbb{M}_d := \mathbb{R}^d \rtimes S^{d-1} := G/H \tag{43}$$

for $d \in \{2, 3\}$, with roto-translation group $G = SE(d) = \mathbb{R}^d \rtimes SO(d)$ and with subgroup $H = \{\mathbf{0}\} \times \mathrm{Stab}_{SO(d)}(\mathbf{a})$. Here $\mathrm{Stab}_{SO(d)}(\mathbf{a}) = \{\mathbf{R} \in SO(d) \mid \mathbf{Ra} = \mathbf{a}\}$ denotes the subgroup of $SO(d)$ that stabilizes an a priori reference axis $\mathbf{a} \in S^{d-1}$.

In case $d = 2$, H consist only of the unity element and $\mathbb{R}^2 \rtimes S^1 \equiv SE(2)$.

Therefore, let us explain the remaining case $d = 3$, where we set $\mathbf{a} = (0, 0, 1)^T$. Then the subgroup H can be parameterized as follows:

$$H = \{h_\alpha := (\mathbf{0}, \mathbf{R}_{\mathbf{a},\alpha}) \mid \alpha \in [0, 2\pi)\}, \tag{44}$$

where we recall, that $\mathbf{R}_{\mathbf{a},\alpha}$ denotes a (counter-clockwise) rotation around the reference axis $\mathbf{a}$. The reason behind this construction is that the group $SE(3)$ acts transitively on $\mathbb{R}^3 \rtimes S^2$ by $(\mathbf{x}', \mathbf{n}') \mapsto g \odot (\mathbf{x}', \mathbf{n}')$ given by:

$$g \odot (\mathbf{x}', \mathbf{n}') = (\mathbf{R}\mathbf{x}' + \mathbf{x}, \mathbf{R}\mathbf{n}'), \qquad \text{for all } g = (\mathbf{x}, \mathbf{R}) \in SE(3),\ (\mathbf{x}', \mathbf{n}') \in \mathbb{R}^3 \rtimes S^2.$$

Recall that by the definition of the left-cosets one has $g_1 \sim g_2 \Leftrightarrow g_1^{-1} g_2 \in H$. The latter equivalence simply means that for $g_1 = (\mathbf{x}_1, \mathbf{R}_1)$ and $g_2 = (\mathbf{x}_2, \mathbf{R}_2)$ one has

$$g_1 \sim g_2 \Leftrightarrow \mathbf{x}_1 = \mathbf{x}_2 \text{ and } \exists_{\alpha \in [0, 2\pi)} \ :\ \mathbf{R}_1 = \mathbf{R}_2 \mathbf{R}_{\mathbf{a},\alpha}.$$

The equivalence classes $[g] = \{g' \in SE(3) \mid g' \sim g\}$ are often just denoted by

$$(\mathbf{x}, \mathbf{n}) \in \mathbb{M}_3.$$

They consist of all $g = (\mathbf{x}, \mathbf{R}_{\mathbf{n}}) \in SE(3)$ that map reference point $(\mathbf{0}, \mathbf{a})$ onto $(\mathbf{x}, \mathbf{n}) \in \mathbb{R}^3 \rtimes S^2 : g \odot (\mathbf{0}, \mathbf{a}) = (\mathbf{x}, \mathbf{n})$, where $\mathbf{R}_{\mathbf{n}}$ is *any* rotation that maps $\mathbf{a} \in S^2$ onto $\mathbf{n} \in S^2$.

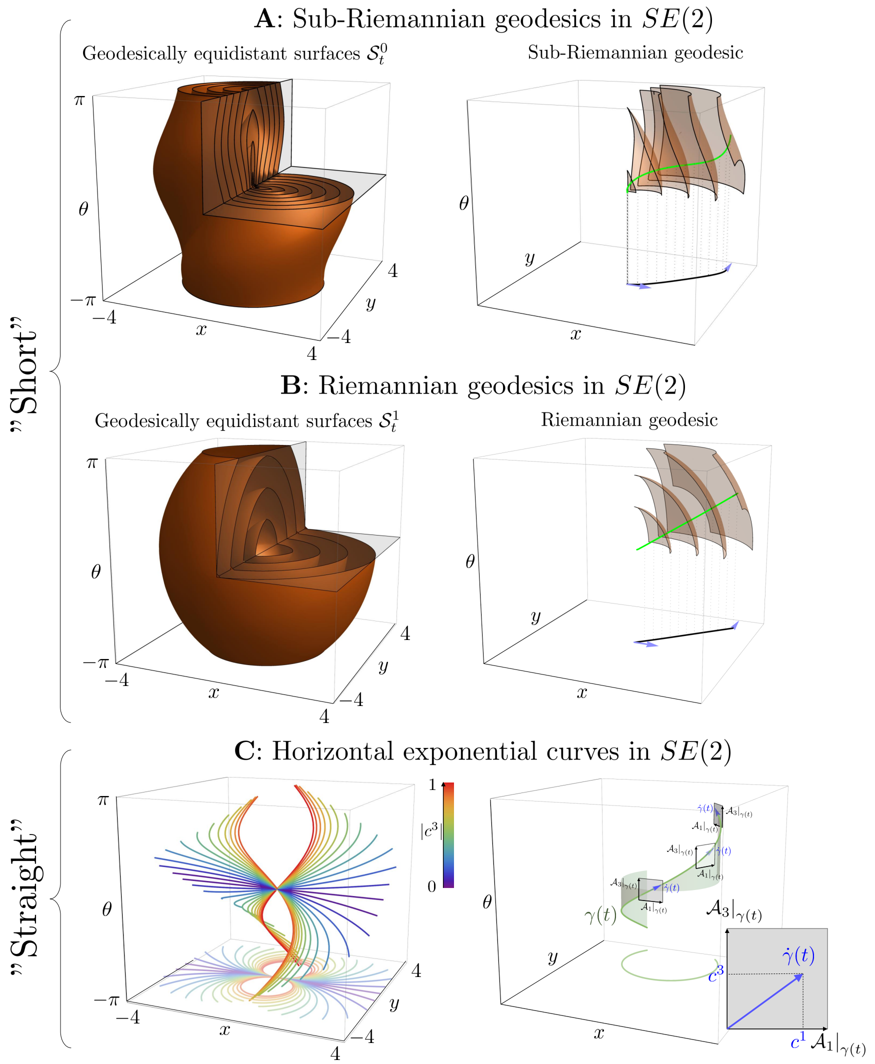

Fig. 7 **A**: Geodesically equidistant surfaces $S_t^\epsilon = \{g \in SE(2) | d_\epsilon(0, g) = t\}$ and geodesic (in green) for the sub-Riemannian case: $\epsilon = 0$ and $C = 1$. **B**: Geodesically equidistant surfaces S_t^ϵ and geodesic for the isotropic Riemannian case: $\epsilon = 1$ and $C = 1$. Now the geodesics are straight lines. **C**: A set of horizontal exponential curves for which $\dot{\gamma}(\tau) = c^1\ \mathcal{A}_1|_{\gamma(\tau)} + c^3\ \mathcal{A}_3|_{\gamma(\tau)} \in \Delta$, with constant tangent vector components c^1 and c^3. Such curves are auto-parallel ('straight curves' in torqued and curved geometry modeled by Lie-Cartan connection $\nabla^{[1]}$).

5 The Metric Models on $\mathbb{M}_d$: Shortest Curves and Spheres

The shortest curves (distance minimizers) are computed by steepest descent on the distance maps, recall Theorem 1 and Fig. 1. For a visualization of a steepest descent (according to Theorem 1) in the lifted image data defined on $\mathbb{M}_d$ see Fig 8.

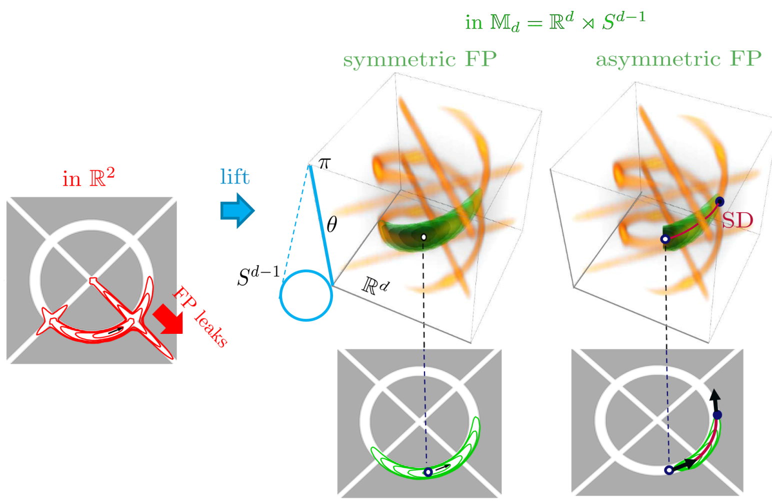

Fig. 8 Geodesic front propagation directly in the image domain leaks at crossings (left). To overcome this complication we lift the data to $\mathbb{M}_d = \mathbb{R}^d \rtimes S^{d-1}$ (here $d = 2$). This gives a mobility/cost C in the lifted space [19, 30]. This determines the distance on (34), and we apply geodesic front propagation (FP) in $\mathbb{M}_d$ via the eikonal equation (40), as depicted by the growing opaque spheres in green. We depict FP in symmetric (sub)-Riemannian models and in asymmetric improvements [19]. In purple we indicate the steepest descent (SD) back-tracking (39).

For uniform cost the non-data driven uniform cost case (i.e. $C = 1$ in (33)) they can be often be computed analytically, and also the cut-locus $t_{cut}(\lambda(0))$ can be computed analytically [65] for $(G = SE(2), \Delta = \text{span}\{\mathcal{A}_1, \mathcal{A}_3\}, \mathcal{G}_0)$.

For the higher dimensional case

$$(G = SE(3), \Delta = \text{span}\{\mathcal{A}_3, \mathcal{A}_4, \mathcal{A}_5\}, \mathcal{G}_0 = \xi^2 \omega^3 \otimes \omega^3 + \omega^4 \otimes \omega^4 + \omega^5 \otimes \omega^5),$$

the curves can be computed analytically [70], and the cut-locus mainly numerically [70, 19]. For an explicit definition of the left-invariant vector fields on $SE(3)$ see Appendix B. The corresponding distance on $\mathbb{M}_3$ is then given by

$$d_{\mathbb{M}_3}(\mathbf{p}_1, \mathbf{p}_2) = \min_{h_1, h_2 \in H} d_{SE(3)}((\mathbf{x}_1, \mathbf{R}_{\mathbf{n}_1})h_1, (\mathbf{x}_1, \mathbf{R}_{\mathbf{n}_2})h_2), \tag{45}$$

where $\mathbf{R}_{\mathbf{n}_i}$ are any rotations mapping a priori reference axis $\mathbf{a}$ onto $\mathbf{n}_i$.

Numerical implementations to compute the shortest distance curves in $d_{\mathbb{M}_d}$ can be done by accurate, relatively slow, PDE-iterations [30], or better by more efficient anisotropic fast-marching algorithms [78] that are sufficiently accurate [79]. For state-of-the-art fast-marching approaches we refer to work of Jean-Marie Mirebeau [78] and several variants including a semi-Lagrangian fast-marching approach (where accuteness of stencils guarantees a single pass algorithm with convergence results) [80]. See also [19]. For a more recent Hamiltonian fast-marching approach see [81]. The Hamiltonian approach directly relates to the PDE-approach in [30] also discretizing the eikonal equations, with the main difference that at each step one updates only the relevant voxels (instead of a full volume) in a single pass algorithm which leads to a tremendous speed up [79].

In practice, it does not make a big difference if one relies on highly anisotropic Riemannian geodesic models (with an anisotropy of say about 10) to simplify sub-Riemannian geodesic models (with infinite anisotropy). See [19, Thm.2] [79] for theoretical and practical underpinning of this statement.

For the homogeneous space of positions and orientations, both the highly anisotropic Riemannian and the sub-Riemannian model have major benefits over isotropic Riemannian models in vessel tracking applications [82, 52], see Section 7.

Furthermore, there exist several extensions of the highly anisotropic Riemannian or sub-Riemannian models [19]. There the most relevant extended models are:

- The **anisotropic, asymmetric, positive control variant** where one forces positive spatial control (see Figure 8) to avoid the problem of cusps (see Figure 9). Essentially it means that the metric tensor fields in (42) are replaced by the following Finsler functions on $T(\mathbb{M}_d)$:

$$\mathcal{F}_0^+(\mathbf{p},\dot{\mathbf{p}})^2 := \begin{cases} \xi^2 |\dot{\mathbf{x}}\cdot\mathbf{n}|^2 + \|\dot{\mathbf{n}}\|^2 & \text{if } \dot{\mathbf{x}} \propto \mathbf{n} \text{ and } \dot{\mathbf{x}}\cdot\mathbf{n} \geq 0, \\ +\infty & \text{otherwise,} \end{cases} \tag{46}$$

  with $\mathbf{p} = (\mathbf{x}, \mathbf{n})$ and $\dot{\mathbf{p}} = (\dot{\mathbf{x}}, \dot{\mathbf{n}})$, and while including a highly anisotropic Riemannian approximation and the mobility/cost C (recall (33) and (34)) into the Finsler function one obtains altogether:

$$\mathcal{F}_\zeta^+(\mathbf{p},\dot{\mathbf{p}})^2 := (C(\mathbf{p}))^2 \left(\xi^2 |\dot{\mathbf{x}}\cdot\mathbf{n}|^2 + \frac{\xi^2}{\zeta^2}\|\dot{\mathbf{x}}\wedge\mathbf{n}\|^2 + (\tfrac{1}{\zeta^2} - 1)(\dot{\mathbf{x}}\cdot\mathbf{n})_-^2) + \|\dot{\mathbf{n}}\|^2\right) \tag{47}$$

  with $0 < \zeta \ll 1$. For details and illustrations see [19].
- **The projective line bundle variant** (where anti-podal points are identified) that partly resolves the cusp-problem [52, ch.4], and that better relates to cortical sub-Riemannian models [69]. It can be shown that it boils down to taking the minimum distance over the four cases that arise by flipping (i.e. $\mathbf{n}_i \mapsto -\mathbf{n}_i$) or not flipping the two boundary conditions. For details see [52].

In Figure 10 we depict growing spheres of several models. It can be observed in the sub-Riemannian setting such spheres reveal folds which is the closure of the first Maxwell set where two geodesics with equal length meet. This is easily understood

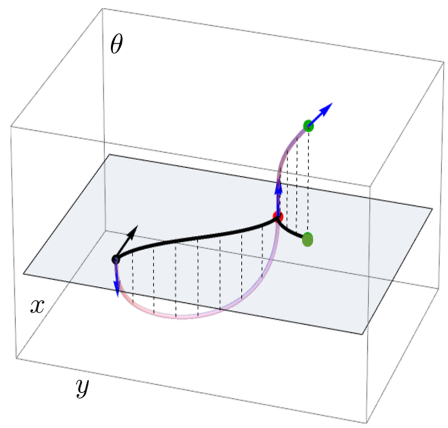

Fig. 9 An example of a smooth sub-Riemannian geodesic $\gamma = (x(\cdot), y(\cdot), \theta(\cdot))$ (in purple), whose spatial projection (in black) shows a cusp (red point). A cusp point is a point (x, y, θ) on γ such that the velocity (black arrow) $\dot{\mathbf{x}}$ of the projected curve $\mathbf{x}(\cdot) = (x(\cdot), y(\cdot))$ switches sign at (x, y).

as geodesic back-propagation via steepest-descent (with the same speed) can be done along two directions orthogonal to each of the orthogonal wavefronts that meet at folds on the spheres. In Figure 11 we depict the cut-locus where geodesic fronts loose their optimality for the projective line bundle case.

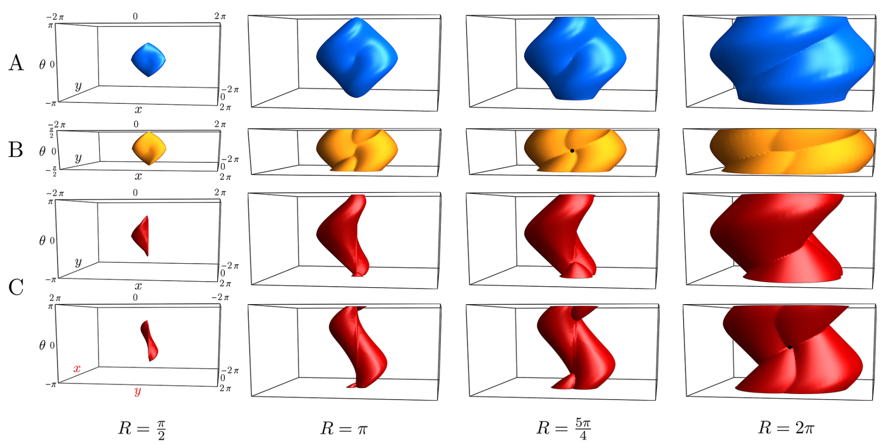

Fig. 10 The development of spheres centered around $\mathbf{e} = (0, 0, 0)$ with increasing radius R. **A:** the normal SR spheres on $\mathbb{M}_2$ given by $\{\mathbf{p} \in \mathbb{M} \mid d_{\mathcal{F}_0}(\mathbf{p}, \mathbf{e}) = R\}$ where the folds reflect the first Maxwell sets [30, 65]. **B:** the SR spheres with identification of antipodal points with additional folds (1st Maxwell sets) due to π-symmetry. **C:** the asymmetric Finsler norm spheres given by $\{\mathbf{p} \in \mathbb{M} \mid d_{\mathcal{F}_0^+}(\mathbf{p}, \mathbf{e}) = R\}$ visualized from two perspectives with extra folds (1st Maxwell sets) at the back $(-\mu, 0, 0)$. The black dots indicate points with two folds. For details see [19].

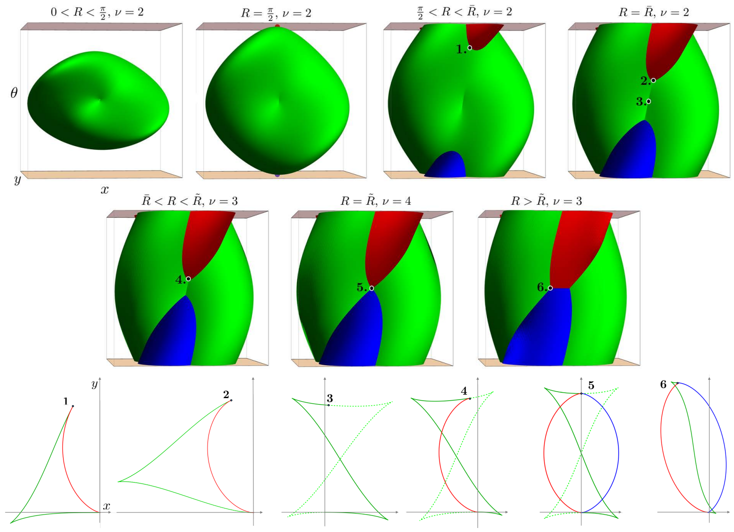

Fig. 11 Top two rows: Evolution of the first Maxwell set as the radius R of the SR-spheres (with uniform cost $C = 1$) increases. First Maxwell sets ar visible via folds on the spheres, as steepest descent (39) has more than one equal length options. Bottom: Equal length SR length minimizers (shortest curves) in the projective line bundle case ending at the points indicated in the top two rows. the multiplicity of the Maxwell-points is indicated by ν and the characteristic radii $\overline{R}$, $\tilde{R}$, where the multiplicity changes from 2 to 3 and from 3 to 4 can be computed analytically, see [52].

6 Straight Curve Fits

Let G be the roto-translation Lie group $G = SE(d) = \mathbb{R}^d \rtimes SO(d)$. Given differentiable data $f : G \to \mathbb{R}$ and a point $g \in G$ we consider the exponential curve $t \mapsto \gamma_{g,\mathbf{c}}(t)$ passing through g at time $t = 0$ with tangent $\gamma'_{g,\mathbf{c}}(0) = \mathbf{c} \in T_g(G)$.

Definition 5 Let $g \in G$. Let $t \geq 0$ and let $\mathbf{c} \in T_g(G)$.

$$\gamma_{g,\mathbf{c}}(t) := g \ \exp_G \left((L_{g^{-1}})_* \boldsymbol{c} t \right) \tag{48}$$

Such an exponential curve (recall Figure 7) is determined by $\mathbf{c} = \sum_{i=1}^{n} c^i \ \mathcal{A}_i|_g \in T_g(G)$. Expressed in the left-invariant moving frame of reference we have

$$\begin{cases} \frac{d}{dt}\gamma_{g,\mathbf{c}}(t) = \sum\limits_{i=1}^{n} c^i \ \mathcal{A}_i|_{\gamma_{g,\mathbf{c}}(t)}, & t \in \mathbb{R}, \\ \gamma'_{g,\mathbf{c}}(0) \quad = \mathbf{c} \in T_g(G). & \end{cases}$$

The tangent to the locally best fitting exponential curve will be the first vector of our locally adaptive frame (henceforth referred to as ‘gauge frame’). The mathematical details on the fitting procedure on how to compute the best fitting exponential curve, and the local optimization problem that defines such a best exponential curve fit will follow in Section 6.1. For now, to get a geometrical intuition, see Figure 12. Inclusion of such a gauge frame has the following benefits:

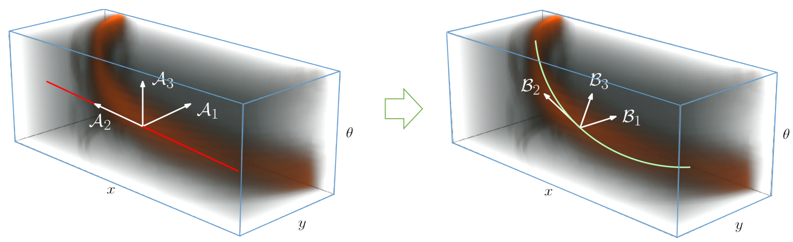

Fig. 12 Illustrating gauge frame fitting at a fixed point $g \in SE(2)$. Top: left invariant frame where $\mathcal{A}_d = \boldsymbol{n} \cdot \nabla_{\mathbb{R}^2}$, as indicated by the red line. Bottom: we choose a frame with $\mathcal{B}_d = \mathbf{c}$ given by (51) or (55) that takes into account the local curvature. In green we see the corresponding exponential curve fit $\gamma_{g,\mathbf{c}}$ to the data.

- It allows for curvature adaption in crossing-preserving PDE-enhancements [83] and curvature estimation in 2D [21] that can be employed for biomarkers of diabetes (see Subsection 7.2) and 3D [84].
- It allows for a reduction of orientation samples [21] (even to $N = 4$) in $SE(2, N) = \mathbb{R}^2 \rtimes \mathbb{T}_N$, where $\mathbb{T}_N$ is the finite subgroup of $\mathbb{T} \equiv SO(2)$ consisting of N equidistant samples on the circle/torus. The reason for this is that it can remove bias towards sampled orientations, as it takes into account deviation from horizontality [85]. Similar considerations apply to the $SE(3)$ setting [45].
- More effective geometric vessel segmentation algorithms [17].

Next we revise the technical considerations in [16] in a coordinate-free way. The considerations in [16] are more general, as it discusses exponential curve fits of the first order (solved by spectral decomposition of a structure tensor of f) and exponential curve fits of the second order. The latter are either solved by spectral decomposition of a symmetric sum of the non-symmetric Hessian of f, or they are solved by spectral decomposition of a symmetric product of the Hessian of f.

Here we shall only be concerned with second order exponential curve fits solved by spectral decomposition of the symmetric product of the Hessian, i.e. by a Singular Value Decomposition (SVD) of the Hessian Hf of f.

Let us remark up-front that a Hessian depends on the choice of connection ∇ on $T(G)$ (inducing a dual connection ∇^* on $T^*(G)$), since by definition [58] one has:

$$Hf = \nabla^* \mathrm{d}f \tag{49}$$

for all $f \in C^2(G, \mathbb{R})$. It will turn out in Section 6.1 that the theory of best exponential curve fits of second order, will boil down to an SVD of $\nabla^* \mathrm{d}f$, where one can either choose $\nabla = \nabla^{[0]}$ or $\nabla = \nabla^{[1]}$ as the corresponding linear maps associated to the Hessian are each other's adjoints. Indeed a brief computation in the frame $\{\mathcal{A}_i\}_{i=1}^n$

of left-invariant vector fields gives us

$$
\begin{aligned}
\left((\nabla^{[0],*})_{\mathcal{A}_i}\mathrm{d}f\right)(\mathcal{A}j) &= \mathcal{A}_i\mathcal{A}_j f,\\
\left((\nabla^{[1],*})_{\mathcal{A}_i}\mathrm{d}f\right)(\mathcal{A}j) &= \mathcal{A}_i\mathcal{A}_j f - \sum_{k=1}^{n} c_{ij}^{k}\mathcal{A}_k f = \mathcal{A}_i\mathcal{A}_j f - (\mathcal{A}_i\mathcal{A}_j - \mathcal{A}_j\mathcal{A}_i)f\\
&= \mathcal{A}_j\mathcal{A}_i f,
\end{aligned}
\tag{50}
$$

where i is the row-index and j is the column-index.

6.1 Exponential Curve Fits of 2nd Order are found by SVD of the Hessian

In this section we will show that exponential curve fits (like the white line in Figure 12) are computed by Singular Value Decomposition of the Hessian. This technique is well-known on the Lie group $G = \mathbb{R}^2$ and widely used in image processing to compute locally adaptive frames (or 'gauge frames') [86] but generalizing this to a Lie group like $G = SE(2)$ requires the Lie-Cartan connections (for $\nu = 0$ or $\nu = 1$ as we will see).

We start by defining the main gauge vector (by means of the Lie-Cartan connection) as:

$$
\mathcal{B}_d\big|_g := \underset{\substack{\mathbf{c}\in T_g(G)\\ \|\mathbf{c}\|=1}}{\operatorname{argmin}} \left\|\left(\nabla^{[0]}_{\mathbf{c}}\mathrm{grad}f\right)(g)\right\|, \tag{51}
$$

where the (metric-intrinsic) gradient is given by the vector field $\mathrm{grad}f = \sum_{i=1}^{n}\xi_i^{-2}(\mathcal{A}_i f)\mathcal{A}_i$. Note that by direct computations one has

$$
\begin{aligned}
\mathcal{B}_d\big|_g &= \underset{\substack{\mathbf{c}\in T_g(G)\\ \|\mathbf{c}\|=1}}{\operatorname{argmin}} \left\|\left(\nabla^{[0]}_{\mathbf{c}}\mathrm{grad}f\right)(g)\right\|\\
&\overset{\text{Lemma 2}}{=} \underset{\substack{\mathbf{c}\in T_g(G)\\ \|\mathbf{c}\|=1}}{\operatorname{argmin}} \left\|\lim_{t\to 0}\frac{\left(L_{g\gamma_{g,\mathbf{c}}(t)^{-1}}\right)_*\ \mathrm{grad}\,f\left(\gamma_{g,\mathbf{c}}(t)\right) - \mathrm{grad}\,f(g)}{t}\right\|\\
&\overset{(9)}{=} \underset{\substack{\mathbf{c}\in T_g(G)\\ \|\mathbf{c}\|=1}}{\operatorname{argmin}} \left\|\sum_{i,j=1}^{n}(\xi_j)^{-2}c^{i}\mathcal{A}_i\mathcal{A}_j f(g)\,\mathcal{A}_j|_g\right\|.
\end{aligned}
$$

Above the vectors in the purple parts belong to $T_g(G)$, whereas the vectors in the green part belongs to $T_{\gamma_{g,\mathbf{c}(t)}}(G)$.

Next we write (51) as a SVD-problem that involves the Hessian of f at g:

$$\begin{aligned}\mathcal{B}_d\Big|_g &= \underset{\substack{\mathbf{c}\in T_g(G)\\ \|\mathbf{c}\|=1}}{\operatorname{argmin}} \|\nabla^{[0]}_{\mathbf{c}}\mathrm{d}f(g)\|_* \\ &= \underset{\substack{\mathbf{c}\in T_g(G)\\ \|\mathbf{c}\|=1}}{\operatorname{argmin}} \|(H^{[0]}f(g))(\mathbf{c},\cdot)\|_*.\end{aligned} \tag{52}$$

Now identify the Hessian $H^{[\nu]}f(g)$ in the natural way to the associated linear map $A_g : T_g(G) \to T_g^*(G)$ by

$$A_g\mathbf{c} := (H^{[\nu]}f(g))(\mathbf{c},\cdot).$$

Then by Euler-Lagrange we have

$$A_g^* A_g \mathbf{c} = \lambda_{min}\mathbf{c} \in T_g(G). \tag{53}$$

so we arrive at an SVD of A.

Remark 12 The SVD values of A^* coincide with the SVD of values A, and one can replace the choice $\nu = 0$ in (52) and (51) with our special choice $\nu = 1$ (which boils down to switching the order of the second order derivatives). Recall also (19).

Remark 13 The matrix representation for (53) relative to the basis of left-invariant vector fields gets a bit involved if expressed in the left-invariant frame since the adjoint A^* depends on the choice of left-invariant metric. In our special case of interest (42) we set $\zeta = 1$ and for $\nu = 1$ we get

$$M_\xi \mathbf{H}^T M_\xi^2 \mathbf{H}\overline{\mathbf{c}} = \lambda_{min}\overline{\mathbf{c}}$$

with $\overline{\mathbf{c}} = M_\xi \mathbf{c}$, and with $M_\xi = \operatorname{diag}\{\xi^{-1}, \xi^{-1}, 1\}$ and with $\mathbf{H}$ the matrix whose element H^i_j with row index i and column index j equals $H^i_j = \mathcal{A}j\mathcal{A}_i f(g)$.

6.1.1 Inclusion of External Regularization

It is also possible to include (external) regularization. For this we need to define neighboring exponential curves.

Definition 6 Let $g, h \in G$. Let $t \geq 0$ and let $\mathbf{c} \in T_g(G)$.

$$\gamma^h_{g,\mathbf{c}}(t) := hg^{-1}\,\gamma_{g,\mathbf{c}}(t) = h\,\exp_G\left((L_{g^{-1}})_*\boldsymbol{c}t\right) \tag{54}$$

$$\mathcal{B}_d\Big|_g := \underset{\substack{\mathbf{c}\in T_g(G)\\ \|\mathbf{c}\|=1}}{\operatorname{argmin}} \left\| \int_G K_\rho\left(h^{-1}g\right)\cdot\left(L_{gh^{-1}}\right)_*\left(\nabla^{[0]}_{\overline{c}}\operatorname{grad} f\right)(h)\;\mathrm{d}\mu(h) \right\|. \tag{55}$$

where μ is the left-invariant Haar-measure on $G = SE(3) = \mathbb{R}^3 \rtimes SO(3)$, with $\overline{c}(h) = (L_{hg^{-1}})_*\mathbf{c} \in T_h(G)$, and where K is an external regularization kernel with tow regularization parameters $\rho = (\rho_S, \rho_A) \in (\mathbb{R}^+)^2$. Typically, it is the direct product of an isotropic spatial Gaussian on $\mathbb{R}^3$ with spatial scale $\rho_S > 0$ and a heatkernel on $SO(3)$ with angular scale ρ_A, for details and motivation see [16, ch:2.7].

Such a regularization will stabilize the best exponential curve fits, so that they become more adjacent with neighboring exponential curve fits. Again the regularized problem is solved with an SVD with A^ρ

$$(A_g^\rho)^* A_g^\rho \mathbf{c} = \lambda_{min} \mathbf{c} \in T_g(G), \text{ with } A_g^\rho = (K_\rho * A_\cdot)(g),$$

which is the regularized version of A (with $A^\rho \to A$ as $\rho \downarrow 0$).

6.1.2 A Single Exponential Curve Fit gives rise to a Gauge Frame

Each local exponential curve fit at $g \in SE(d)$ to lifted data (orientation score) gives rise to a basis of local derivatives ('gauge frame'). This can be seen for $d = 2$ in Figure 12. The general mathematical construction is explained in [16, App.A, Thm. 7], and is highly beneficial in medical imaging applications (such as in vessel segmentation, see [17] for extensive comparisons to many other geometric and machine learning methods). For documented implementations of Gauge frames in $SE(d)$, for $d = 2, 3$, in *Mathematica* see [50].

7 Overview of Image Analysis Applications for $G = SE(d)$

The analysis and computation of intensity variations in images plays a fundamental role in image processing. Here it is particularly useful to employ orientation lifts such as orientations scores [3, 48, 87], continuous wavelet transforms [1, 38, 88], or orientation channel representations [5, 6], to take advantage of the manifest disentanglemant of local orientations in images to deal with complex structures such as crossings, recall Fig. 1.

For example, the crossing-preserving geometric analysis could be in solving PDE flows for enhancement [45, 14, 13, 39], denoising [10], regularization [24], perception [1, 87], or segmentation [17], for determining principal directions [16] (e.g. to steer PDEs or filters [89]), or for defining geometric regularization priors in machine learning [82, 32].

In the up-coming sub-sections we go through some of the applications which find a direct application of the theory described in this chapter. Some algorithms based on the described differential geometric toolset on $\mathbb{M}_d$ can be regarded as the natural generalization of classical geometric tools on $\mathbb{R}^d$. For example the widely used Frangi vesselness filter [90] is based on the analysis of the Hessian, which in our framework of lifted representations via orientation scores [89] is computed via an SVD of the Hessian induced by the the Lie-Cartan connection with $\nu = 1$ recall Section 6.

More important, however, is that the proposed toolset enables the design of a completely new range of algorithms that enables analyses that are simply not possible by holding on to data representations on $\mathbb{R}^d$. These include globally optimal path optimization with an intrinsic (curvature penalizing) smoothness constraint via sub-Riemannian geometry [30, 19, 91, 81, 92], which is the topic of Section 7.1; the direct computation of curvature and torsion of blood vessels for biomarker research without having to explicitly track/model the vessel trajectories [18], which is the topic of Section 7.2; and crossing-preserving, curvature-adaptive denoising schemes [25, 10, 41], which is the topic of Section 7.3.

What all of these applications have in common is that they either rely on 'straight curves' which are auto-parallel w.r.t. the Lie-Cartan connections or on 'shortest curves' which have parallel momentum (for $\nu = 1$) according to our main theorem, Theorem 1.

The differential-geometrical toolset described in this chapter can directly be translated to numerical schemes by working with discrete grids and finite difference stencils [93], or via basis expansion methods such as spherical harmonics [84, 94, 95] and B-splines [82] that allow for the computation of exact derivatives, or via a mix of numerical and analytical schemes [4, 9]. Examples of the latter include the use of analytic approximations of sub-Riemannian distances [65, 30] in a clustering algorithm [96], or analytic solution approximations to left-invariant diffusion equations [97] for smoothing or uncertainty analysis [27]. The interested reader is referred to [25, 84, 16, 93, 4] for algorithmic implementation details of the left-invariant derivatives for processing of orientation scores.

7.1 Shortest Curve Application: Tracking of Blood Vessels

Shortest path algorithms provide a robust way of extracting trajectories of blood vessels in medical images in a semi-automatic way. They rely on the specification of start and end points of the curves by a user, after which the algorithm computes the globally optimal geodesic connecting these points given a pre-computed metric. A fundamental problem in such algorithms is, however, that they have difficulties in tracking blood vessels through complex geometries, and that they suffer from so-called short cuts in which the computed geodesics snap to parallel vessels or other interfering structures, see e.g. Fig. 13. Via the computation of shortest paths in the lifted space $\mathbb{M}_d$ using a sub-Riemannian geometry (cf. Fig. 1) we are able to solve such limitations of classical vessel tracking on $\mathbb{R}^d$.

In our approach for computing globally optimal sub-Riemannian distance minimizers between two points $g_0, g_1 \in SE(2)$ we consider the metric $d_{\mathcal{G}_0}$ of Eq. (34), which is defined using the SR metric tensor $\mathcal{G}_0$ given in (30) and which is based on a cost function $C : G \to \mathbb{R}^+$ that is derived from the orientation score. The cost function encourages curves to move over vessel regions (low cost) and penalizes moving over background regions (high cost). Such a cost can for example be derived from the orientation score via a vesselness measure [89], a line-fidelity measure based on left-invariant derivatives [30] or gauge derivatives in $SE(2)$ [16, 17]. The actual computation of the shortest paths then consists of 1) solving the SR Eikonal equation in order to obtain a distance map from g_0 to any other point in $SE(2)$ and 2) perform gradient descent on the distance maps from g_1 back to g_0 to obtain the geodesic (cf. Theorem 1). The numerical computation of step 1 can for example be done in an iterative up-wind scheme with left-invariant finite-difference stencils [30], or via very efficient Fast Marching schemes [81, 80] in which the sub-Riemannian metric tensor field is approximated with a highly anisotropic Riemannian metric tensor field [79].

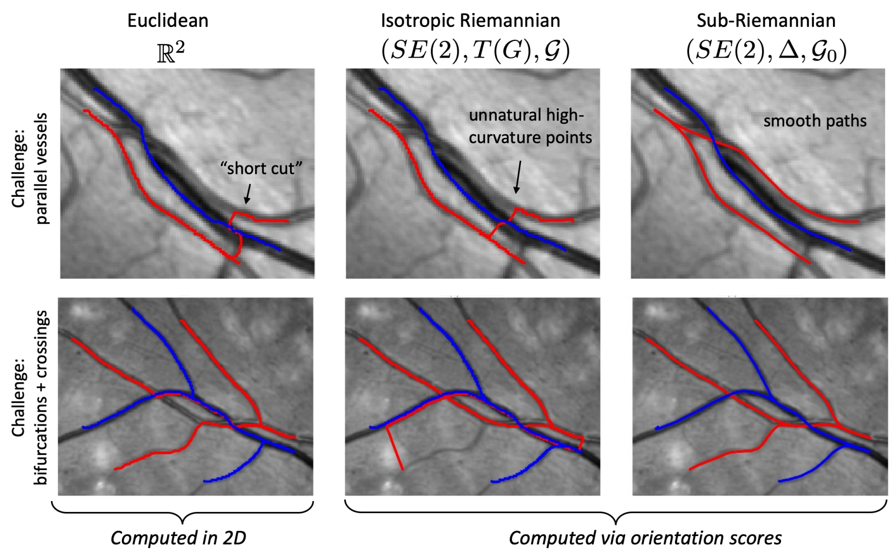

Fig. 13 Results of globally optimal data-adaptive geodesics computed in different metric tensor settings. Left column: Conventionally such shortest paths are computed based on 2D isotropic metrics. Such models suffer from short cuts (geodesics snap to other, typically parallel, dominant vessels) and often fail at crossings. Middle column: Shortest path computations using an isotropic metric in a lifted position-orientation space $\mathbb{M}_2 \equiv SE(2)$ reduces problems with crossings due to a disentanglement of local orientations, but the issue of short cuts remains as unnatural curves with high curvature points are still allowed. Right column: Both problem are solved by working with a sub-Riemannian metric on $SE(2)$ by which only natural curves are allowed in the lifted space (cf. Fig. 1). The right two columns show the 2D projections of geodesics in $SE(2)$. For further experiments on large datasets see [30, 52].

Exemplary results are given in Fig. 13 and a quantitative evaluation of the benefit of a sub-Riemannian versus Riemannian metrics is given in Tbl. 1. The principle that in a sub-Riemannian framework we only consider natural smooth paths, as illustrated in Fig. 1, leads to very clear improvements for vessel tracking. The method for computing such curvature-penalized data-adaptive SR geodesics generalizes well to other Lie groups G and has found several high-impact applications in medical

Table 1 Comparison of successful vessel extractions [96] via Riemannian geodesics using 2D isotropic metric tensors in the image domain, Riemannian geodesics in the lifted domain $SE(2)$ of orientation scores with spatially isotropic metric tensors, and sub-Riemannian geodesics in $SE(2)$

Metric	Nr of successful vessel extractions
Riemannian $\mathbb{R}^2$	71.7% (132/184)
Riemannian $SE(2)$ - Eq. (33)	82.6% (152/184)
Sub-Riemannian $SE(2)$ - Eq. (34)	92.4% (170/184)

image analysis. See e.g. [30, 79] for 2D vessel tracking via SR-geodesics in $G = SE(2)$. See also [37] for vessel tracking in retinal images defined on the 2-sphere $S^2 = SO(3)/SO(2)$ via SR-geodesics in $SO(3)$.

7.1.1 Shortest Curve Applications: Geodesic Vessel and Fiber Tracking in $\mathbb{M}_3$

In [19] the anisotropic and sub-Riemannian geodesic tracking theory was developed and extended with more general Finslerian models such as the one given in (46). These Finsler models were called variants of the 'Reeds-Shepp Car Model'. Some of these models turn off the reverse gear of the car and tackle the problem of cusps (recall Fig. 9) that can appear in spatial projections of sub-Riemannian geodesics. In [19] the underlying theory was also extended to 3D (or more precisely to the five dimensional homogeneous space $\mathbb{M}_3$ of positions and orientations). It has led to efficient perceptional grouping methods [96] where vascular trees are constructed from the separate geodesic tracts following 3D blood vessels. When extending the models from the 3D manifold $\mathbb{M}_2$ to the 5D manifold $\mathbb{M}_3$ it is crucial to rely on fast anisotropic fast-marching methods [98] that do approximate the sub-Riemannian setting (with infinite anisotropy) reasonably well, as shown by comparison [19] to the exact sub-Riemannian geodesics in $\mathbb{M}_3$ derived in [70]. The idea of using highly anisotropic, advanced, fast-marching methods by Mirebeau [98, 80] to approximate sub-Riemannian geodesics was proposed by Sanguinetti et al. [79] on $\mathbb{M}_2$, where numerical comparisons reveal enormous speed-ups (compared to iterative PDE-techniques in [30, 99]) while maintaining a neglectable loss of accuracy. It was employed for crossing-preserving fiber tracking [99, 19], and for crossing-preserving structural connectivity measures [100] (between anatomical regions of interest) in DW-MRI data of the brain (in response to earlier work by Pechaud et al. [101]).

Since, our previous works [30, 19] mainly concentrated on tracking of 2D blood vessels in optical images, and 3D neural fiber tracking in DW-MRI [100, 19], we show a 3D vessel tracking experiment in this book chapter. See Figure 14. Again we recognize the benefit of the asymmetric version (46) of the 3D sub-Riemannian geometrical model on the lifted space $\mathbb{M}_3$ over the corresponding isotropic Riemannian geodesic model on $\mathbb{M}_3$, and over the corresponding geodesic model on $\mathbb{R}^3$. The new model does not suffer from nearby elongated structures, does not take wrong exits (as shown in [19]), deals with bifurcations by 'keypoints' (in place rotations), and produces less oscillatory tracts due to the sub-Riemannian geometry (that does not allow for direct side-ward motions in contrast to the blue 'shaky' tract in Fig. 14).

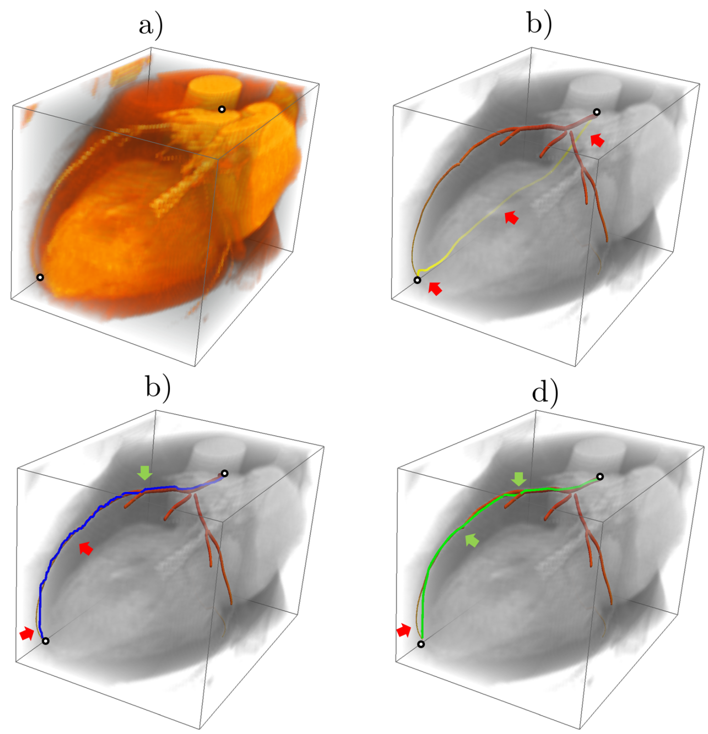

Fig. 14 Tracking of coronary arteries in 3D-X-ray: a) test-data set with two boundary points $\mathbf{x}_0, \mathbf{x}_1 \in \mathbb{R}^3$, b) geodesic tracking result (yellow) that is far from ground truth (red) when applying standard geodesic tracking [102] on $\mathbb{R}^3$ without lifting to $\mathbb{M}_3$, c) geodesic tracking result (blue) when applying geodesic tracking in $\mathbb{M}_3$ using the isotropic Riemannian model (i.e. using Finsler function $\mathcal{F}(\dot{\mathbf{x}}, \dot{\mathbf{n}}) = \sqrt{\xi^2\|\dot{\mathbf{x}}\|^2 + \|\dot{\mathbf{n}}\|^2}$ with ξ=0.1), d) geodesic tracking result when applying geodesic tracking in $\mathbb{M}_3$ using the sub-Riemannian model (i.e. using asymmetric Finsler function $\mathcal{F}_0^+$ given by (46) again with $\xi = 0.1$). The spherical parts of the boundary conditions $\mathbf{p}_1 = (\mathbf{x}_1, \mathbf{n}_1)$ and $\mathbf{p}_2 = (\mathbf{x}_2, \mathbf{n}_2)$ in (45) are automatically optimized by checking for the 'first passing front'. I.e. adjust the source set in eikonal PDE system (40) in Theorem 1 from singleton $\{e\}$ to the set $\mathcal{S} = \{(\mathbf{x}_0, \mathbf{n}) \mid \mathbf{n} \in S^2\}$ and select minimal $\mathbf{n}_1 = \mathrm{argmin}_{\mathbf{n}\in S^2} W(\mathbf{x}_1, \mathbf{n})$ prior to back-tracking (39).

Furthermore, we note that non-data-adaptive sub-Riemannian distances in $SE(d)$ can be efficiently computed using analytic approximations [12, 97, 103] which can be used in real-time clustering of local orientations for perceptual grouping of blood vessels [96], or in morphological convolutions in equivariant deep learning [32].

Finally, for detailed evaluations and experiments of geodesic tracking in $\mathbb{M}_3$, we refer to [100, 19] where the experiments are focused on fiber tracking in DW-MRI.

7.2 Straight Curve Application: Biomarkers for Diabetes

The total amount of curvature/torsion of blood vessels, which is often summarized in a single tortuosity measure, is associated with severity of several systematic diseases such as diabetes and hypertension [18, 4, 104, 105, 106]. Reliable and automatic quantification of tortuosity is therefore a high value aid in the automatic early diagnosis of such systemic diseases and in the study of disease progression via large scale cohorts. The theory of exponential curve fits in $SE(d)$ enables a unique approach to the quantification of tortuostity in retinal images, which is both robust, reliable and fast [18]. Retinal images are obtained by optical devices [4] and thereby provide an easy non-invasive way to image the quality of blood vessels.

As described in Sec. 6, it is possible to locally fit exponential curves (see e.g. Fig. 12 and Fig. 15) to the orientation score data $U := \mathcal{W}_\psi f : \mathbb{M}_2 \to \mathbb{R}$ of a retinal image $f : \mathbb{R}^2 \to \mathbb{R}$ via an SVD of left-invariant Hessian $\nabla^{[1],*}\mathrm{d}U$. This is akin to fitting straight lines to local intensity patterns in images, underlying classical vesselness measures in [90]. The exponential curves in $SE(d)$ are equally 'straight', but now with respect to the torqued geometry modeled by Lie-Cartan connection $\nabla^{[1]}$, recall Theorem 1. This torqued geometry is also visible in an orientation score, recall Fig. 1 and see Fig. 7. These 'straight' curves have constant velocity components w.r.t. the left-invariant frame $\{\mathcal{A}\}_{i=1}^n$, and their projections to $\mathbb{R}^d$ are circles/spirals whose curvature κ can directly be computed. E.g., in $SE(2)$ one has $\kappa = \frac{c^3 \operatorname{sign} c^1}{\sqrt{|c^1|^2+|c^3|^2}}$.

Akin to the vessel enhancement techniques via orientation scores of [17, 89], a confidence measure for the presence of a line structure can be extracted from the left-invariant Hessian [107, 25, 18]. Together, the confidence and curvature measure can be used to obtain summarizing statistics for the amount of tortuosity of blood vessels in medical images, as is illustrated in Fig. 15. Such tortuosity measures are significantly associated with severity of diabetes and hypertension on large scale clinical datasets with retinal images [18, 4, 104, 105, 106]. For quantification of blood vessel tortuosity in 3D medical image data see [84].

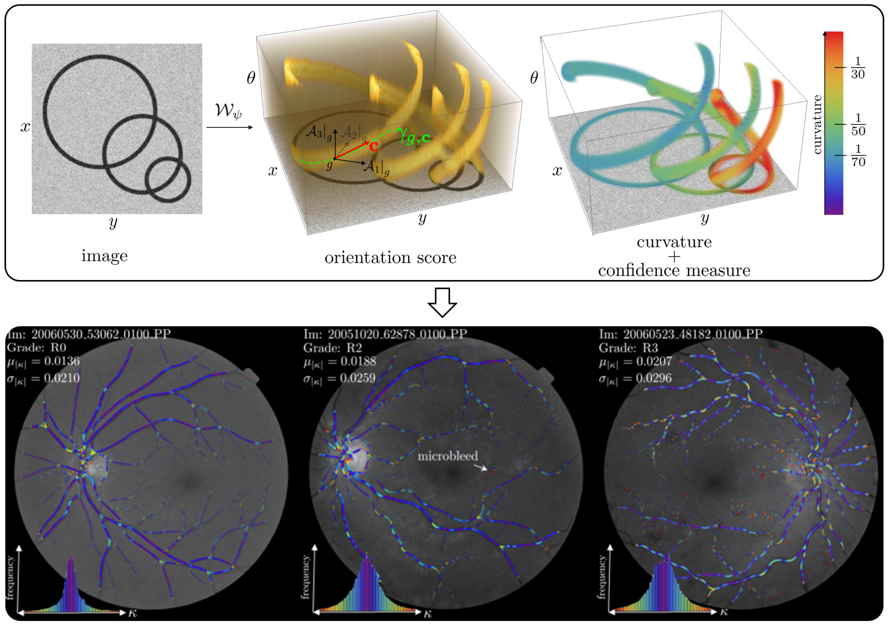

Fig. 15 Top row: Via exponential curve fits in orientation scores (cf. Sec. 6) we are able to locally analyze line structures and compute their corresponding curvature values, as well as assigning confidence scores at each position and orientation. In the right most figure, curvature is color coded and confidence is encoded with opacity. Bottom row: confidence and curvature projected to the 2D plane and visualized as in an overlay on top of the original input image. From these summarizing statistics such as the mean and standard deviation of absolute curvature can be computed, which can be used as biomarkers for diabetes and hypertension.

7.3 Straight Curve Application: PDEs on $\mathbb{M}_2$ for Denoising

Two key ideas have greatly improved techniques for image enhancement and denoising: the lifting of image data to multi-orientation distributions (e.g. orientation scores[42]), and the application of nonlinear PDEs such as Total Variation Flow (TVF) and Mean Curvature Flow (MCF). These two ideas were recently combined by Chambolle & Pock (for TVF)[24] and Citti [1] et al. (for MCF) for 2D images.

In our recent works [10, 41], these approaches were extended to enhance and denoise images of arbitrary dimension. The TV flows and MC flows on $\mathbb{M}_d$ showed best results when using locally adaptive frames of a specific type. Namely, these locally adaptive frames that were computed via the best-exponential curve fit procedure (i.e. the 'straight curve' fit in the torqued and curved space $SE(d)$, recall Theorem 1, and Figs. 1 and 7) explained in Section 6. Then the standard procedure mentioned in Subsection 6.1.2 to compute the induced locally adaptive frame ('gauge frame') $\{\mathcal{B}_1, \ldots, \mathcal{B}_n\}$ is applied. The principle direction $\mathcal{B}_d$ tangent to the exponential curve is computed as the eigenvector with smallest eigenvalue in the SVD of the Hessian induced by the Lie-Cartan connection with $\nu = 1$, recall Definition 6.

For an illustration, recall figure 12 where $d = 2$ and $n = 3$.

In this section we constrain ourselves to $d = 2$ and we shall summarize the MCF & TVF PDEs on $SE(2)$ (for crossing-prerving flows via invertible orientation scores, recall Figure 1) and highlight a denoising result, where we compare to a popular denoising method called 'Block Matching 3D' (BM3D) [108, 109].

The PDE system for MCF & TVF on $\mathbb{M}_2 = SE(2)$ via the gauge frame $\{\mathcal{B}_1, \ldots, \mathcal{B}_3\}$ is best expressed in this frame and is given by:

$$\begin{cases} \frac{\partial W}{\partial t}(g,t) = \|\nabla W(g,t)\|^a \sum_{i=1}^{3} \mathcal{B}_i \left(\frac{\mathcal{B}_i W(\cdot,t)}{\|\nabla W(\cdot,t)\|} \right)(g), & g \in SE(2),\ t \geq 0, \\ W(g,0) = U(g), & g \in SE(2), \end{cases} \tag{56}$$

with parameter $a \in \{0,1\}$, where we have a total variation flow (TVF) if $a = 0$, and a mean curvature flow (MCF) if $a = 1$. We denote the operator that maps the orientation score $U(\cdot)$ to its denoised version $W(\cdot,t)$ by Φ_t:

$$W(g,t) = (\Phi_t(U))(g), \text{ for all } g = (\mathbf{x},\theta) \in SE(2),\ t \geq 0,$$

where we use standard identification $\theta \in \mathbb{R}/(2\pi\mathbb{Z})$ with the corresponding counter-clock wise planar rotation about angle θ.

The initial condition U for our TVF/MCF-PDE (56) is set by an orientation score [3, 48] of image $f : \mathbb{R}^2 \to \mathbb{R}$ given by

$$U(\mathbf{x},\theta) := \mathcal{W}_\psi f(\mathbf{x},\theta) = (\psi_\theta \star f)(\mathbf{x}), \qquad \mathbf{x} \in \mathbb{R}^2, \theta \in \mathbb{R}/(2\pi\mathbb{Z}).$$

where $\star$ denotes correlation and ψ_θ is the rotated wavelet aligned with $(\cos\theta, \sin\theta) \in S^1$. For ψ we use a cake-wavelet [3, 48] $\psi : \mathbb{R}^2 \to \mathbb{R}$ with standard settings [50]. Then we compute:

$$f \mapsto \mathcal{W}_\psi f \mapsto \Phi_t(\mathcal{W}_\psi f)(\cdot,\cdot) \mapsto f_t(\cdot) := \int_{-\pi}^{\pi} \Phi_t(\mathcal{W}_\psi f)(\cdot,\theta)\, \mathrm{d}\theta. \tag{57}$$

for $t \geq 0$. The cake-wavelets allow us to reconstruct by integration over S^1 only [3, 48]. By the invertibility of the orientation score one thereby has $f = f_0$ so due to this reconstruction property the flows depart from the original image at $t = 0$.

Now that the PDEs are set for MCF and TVF and the corresponding image regularization operators $f \mapsto f_t$ via invertible orientation scores are set (by Eq. (57) and (56)) we conclude with a denoising experiment. End-times $t > 0$ are chosen such that relative $\mathbb{L}_2$-error between the original image and its denoised image is minimal.

We test the effect of MCF and TVF on two images polluted with correlated noise: the (monochrome) Mona Lisa and an electron microscopy image of collagen. We compare the performance (in terms of peak-signal-to-noise-ratio) against the BM3D method, see Table 2 for the PSNR values and Figure 16 for a qualitative comparison.

Table 2 Comparing Peak-Signal-to-Noise-Ratio (dB) for the gauge MCF and TVF methods against BM3D (higher is better).

Gaussian noise	Collagen	Mona Lisa
Noisy image	14.1	14.1
Perona-Malik	20.1	20.5
BM3D	23.1	23.9
Left inv. MCF	21.7	23.3
Gauge MCF	21.7	23.7
Left inv. TVF	22.4	26.0
Gauge TVF	**23.0**	**26.1**
Correlated noise	Collagen	Mona Lisa
Noisy image	23.9	23.9
Perona-Malik	24.2	25.1
BM3D	24.0	26.3
Left inv. MCF	23.8	26.2
Gauge MCF	23.9	26.2
Left inv. TVF	24.7	26.8
Gauge TVF	**24.9**	**26.9**

As confirmed by Table 2 and Fig. 16 we observe the following:

- denoising via orientation scores is beneficial over direct image denoising. For PDE-based image processing this was already done in [25], and by others in [13, 1, 2, 110, 87] performing left-invariant PDE-based image processing via 'orientation liftings' (expanding the image domain to $\mathbb{M}_d$). However, our experiments where we use (data-driven) TVF and MCF (56) on $\mathbb{M}_2$, now show that we considerably improve quantitative results in comparison to a general (not necessarily PDE-based) well-performing image denoising method such as BM3D [108, 109].
- best performances are obtained by the Gauge TVF method, i.e. the method applying (57) with Φ_t given by (56) with $a = 0$.
- using the locally adaptive frame $\{\mathcal{B}_i\}$ in (56) increases the performances over their 'normal left-invariant counterparts'. With the normal left-invariant counter parts we mean (57) with Φ_t given by a PDE system on $\mathbb{M}_2 \equiv SE(2)$ that arises from (56) replacing each $\mathcal{B}_i$ in (56) by $\mathcal{A}_i$:

$$\begin{cases} \dfrac{\partial W}{\partial t}(\mathbf{p},t) = \|\nabla W(\mathbf{p},t)\|^a \displaystyle\sum_{i=1}^{3} \mathcal{A}_i \left(\dfrac{\mathcal{A}_i W(\cdot,t)}{\|\nabla W(\cdot,t)\|} \right)(\mathbf{p}), & \mathbf{p} \in \mathbb{M}_2,\ t \geq 0, \\ W(\mathbf{p},0) = U(\mathbf{p}), & \mathbf{p} \in \mathbb{M}_2, \end{cases} \tag{58}$$

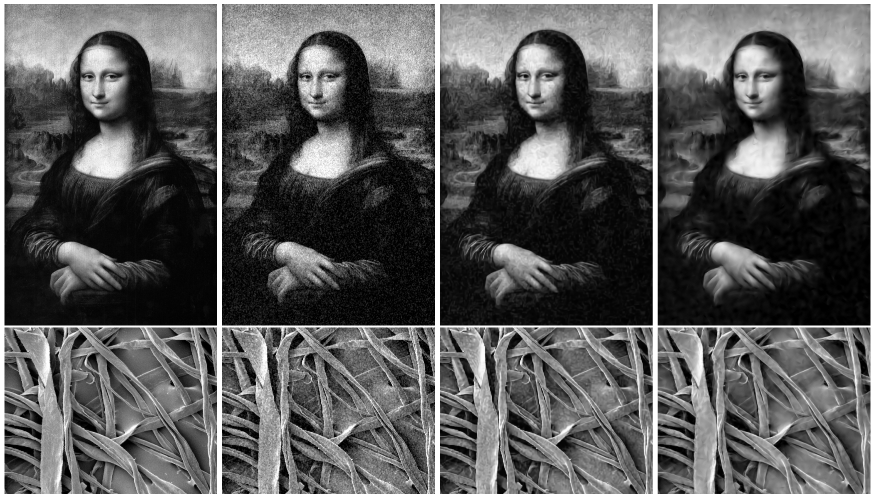

Fig. 16 Comparing Gauge TVF with coherence enhancement and BM3D against correlated noise. Top row, from left to right: 1. original image, 2. original image polluted with correlated Gaussian noise, 3. denoising result using the BM3D method, 4. denoising result using the TVF method via invertible orientation scores given by (57) relying on PDE (56) with $a = 0$. Bottom row, the same as the top row but now applied on a different image containing collagen fibers. The standard deviation for BM3D and evolution time for TVF were adjusted to reach optimal $\mathbb{L}_2$ error, see [41] for details.

as done also in [13, 111]. Gauge TVF performs better than normal left-invariant TVF, Gauge MCF performs better than normal left-invariant MCF via invertible orientation scores (57).

These observations are also supported by much more experiments with both quantitative and qualitative comparisons for the case $d = 2$ and $d = 3$ see [41]. Regarding related works and experiments via crossing-preserving diffusions via invertible orientation scores we refer to [25] ($d = 2$) and [45] ($d = 3$).

In [41] we have compared the (crossing-preserving) TVF and MCF PDE flows via invertible orientation scores to (crossing-preserving) nonlinear diffusions via invertible orientation scores. In general better results are obtained by the MCF and TVF approach than with nonlinear diffusion (Perona-Malik [112], coherence enhancing diffusion [113]). However, edge-enhancing diffusion techniques [114] via invertible orientation scores, could advocate otherwise, and are left for future work.

7.3.1 Straight Curve Application: PDEs on $\mathbb{M}_3$ for Denoising FODFs in DW-MRI

In this subsection we briefly highlight the extensions of the TVF and MCF denoising methods from 3-dimensional manifold $\mathbb{M}_2$ towards 5-dimensional manifold $\mathbb{M}_3$.

Essentially, the MCF flows and TVF flows given in (58) are generalized to $\mathbb{M}_3$ by using the left-invariant vector fields on $\mathbb{M}_3$ instead of the left-invariant vector fields on $\mathbb{M}_2$. In our experiments we optimized the stopping time of the evolutions to get a denoised distribution on $\mathbb{M}_3$. For details see [41]. In [41] (crossing-preserving) TVF and MCF PDE flows on the 5 dimensional manifold $\mathbb{M}_3$ are compared to nonlinear diffusion methods on this manifold such as

- crossing-preserving versions [115] of Perona and Malik (PM) [112] diffusions.
- crossing-preserving versions [12, 39] of coherence enhancing diffusion (CED).

This has been applied to crossing-preserving enhancement and denoising of Diffusion-Weighted MRI (DW-MRI) data, where *fiber orientation density functions* (FODF), cf. [116, 117] are positive, realvalued functions defined on the 5-dimensional space $\mathbb{M}_3$ are similar to orientation scores of 3D image data. To see the similarity compare Fig. 17 to the middle column in Fig. 3. So in this application we only rely on the right part of our commutative diagram in Fig. 2.

Remark 14 (**DW-MRI: application background**)
The idea of diffusion-weighted MRI is to measure angular diffusivity profiles of water molecules that are generally believed to follow the biological fibers in brain white matter. As such it provides a non-invasive way to image the structural connectivity between anatomical regions in the brain. This is important for surgical planning. For example, identifying the optic radiation bundle is important as it is responsible for the visual sight of a patient. In case of severe epilepsy surgery may be applied (e.g. a temporal lobe resection), where surgeons should not damage the optic radiation bundle as this can lead to a reduction of visual sight. Left-invariant PDE-evolutions (such as diffusions) on $\mathbb{M}_3$ discussed in [12, 99, 94, 14, 39] are very beneficial for identifying such bundles, as shown by Meesters et al.[27], and more generally by Prckovska et al [20].

As we can see in Fig. 17, the FODF obtained from raw DW-MRI data via an effective and widely used method CSD produces a lot of spurious peakes in the spatial field of angular distributions that are not well-aligned/supported by neighboring peaks and one needs 'contextual processing' [20, 14, 94] to identify large bundles [26, 27] in a stable way. Here we observe that crossing-preserving MCF and TVF on $\mathbb{M}_3$ better preserve crossings and bundle boundaries than diffusion methods do. For detailed evaluations see [41, 51].

7.3.2 Straight Curve Application: PDEs on $\mathbb{M}_3$ for Denoising 3D X-ray data

Denoising of 3D X-ray data is important as reduction of acquisition time and radiation dose typically leads to noisy X-ray images. In [45] denoising experiments are provided with crossing-preserving nonlinear diffusions on $\mathbb{M}_3$ via invertible orientation scores of 3D X-ray data.

These tests do follow the full commutative diagram in Fig. 4 and applied denoising as depicted in the bottom row of Fig. 3 and provide the $\mathbb{M}_3$-analogue of (57):

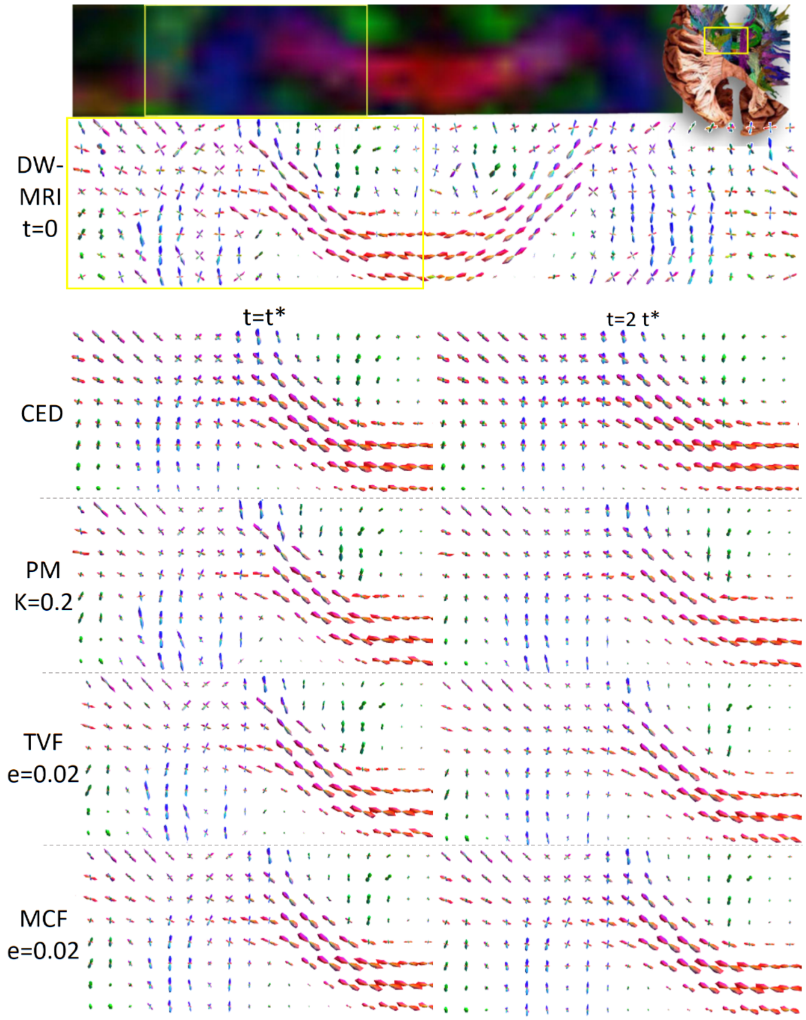

Fig. 17 Qualitative comparison of denoising a FODF obtained by (CSD) [116, 117] from a standard DW-MRI dataset (with $b = 1000s/mm^2$ and 54 gradient directions). For the CSD we used up to 8th order spherical harmonics, and the FODF is then spherically sampled on a tessellation of the icosahedron with 162 orientations. Image is taken from our previous journal article [41]. For details on this qualitative DW-MRI experiment and related quantitative DW-MRI denoising experiments see the works by St.-Onge et al. [51] and Smets et al. [41].

$$f \mapsto \mathcal{W}_\psi f \mapsto \Phi_t(\mathcal{W}_\psi f)(\cdot,\cdot) \mapsto f_t(\cdot) := \int_{S^{d-1}} \Phi_t(\mathcal{W}_\psi f)(\cdot,\mathbf{n})\,\mathrm{d}\sigma(\mathbf{n}). \tag{59}$$

but then with $\Phi_t(U) = W(\cdot,t)$ a nonlinear diffusion process described in gauge frames (relying on a SVD of the Hessian of the orientation scores as explained in Section 6.1) stopped at optimal time $t > 0$. For details see [45, ch:6.1.2]. The preservation of complex structures in vasculature is remarkable, see Fig. 18. For qualitative and quantitative comparisons against many other nonlinear diffusion methods we refer to the work by Janssen et al.[45].

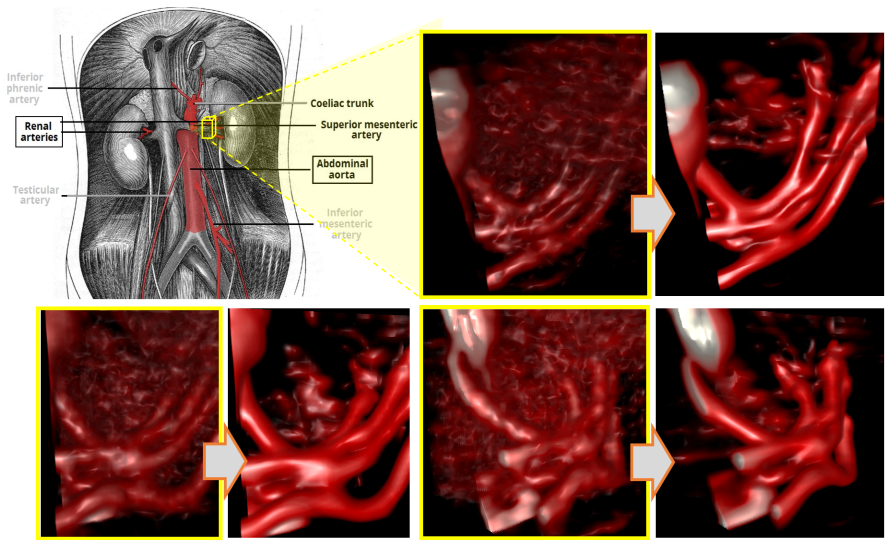

Fig. 18 3D-X ray image of renal arteries. 3 view points on the same scene. Input image in yellow frame, output of coherence enhancing diffusion via 3D-orientation scores (CEDOS: Eq. (59) for a fixed stopping time. For details and comparisons to other methods such as coherence enhancing diffusion [113] acting directly in the image domain see [45].

8 Conclusion

Geometric processing of multi-feature image representations on a Lie group G requires us to 'connect' different tangent spaces in the tangent bundle $T(G)$ by a connection. To this end we studied all Lie-Cartan connections $\nabla^{[\nu]}$ parameterized by $\nu \in \mathbb{R}$. This holds in particular for our case of interest where $G = SE(d)$ (or more precisely the Lie group quotient $\mathbb{M}_d$) and where the score is an orientation score. It turned out by our Theorem 1 that the case $\nu = 1$ is the best choice; shortest curves have parallel momentum whereas straight curves have parallel velocity as intuitively illustrated in Fig. 7. This connection does have torsion with constant coefficients relative to the left-invariant frame and coframe as shown in Lemma 3. It reflects the torsion visible in the domain of an orientation score, see Figure 1.

We studied the shortest curves in $\mathbb{M}_2 \equiv SE(2)$ for different choices of metric tensor fields (or more general: Finsler functions) and computed the corresponding spheres in $\mathbb{M}_2$ in Section 5. Recall Figure 10, where the spheres were computed via the geodesic wavefront propagation technique explained in Theorem 1. Such geodesic wavefront propagations also allow for data-driven versions (via the external cost C that can be adapted to the orientation score). The major benefit of geodesic wavefront propagation in the orientation score domain $\mathbb{M}_d$ over geodesic wavefront propagation in the image domain $\mathbb{R}^d$ is that fronts do not leak at crossings as illustrated in Fig. 8. This explains the clear advantage for subsequent geodesic tracking (via the steepest descent in Theorem 1) in the tracking of blood vessels presented in Section 7.1. Furthermore, we show best results are obtained by the sub-Riemannian model rather than the isotropic Riemannian model. Recall Figure 13.

We studied the straight curves (exponential curves) in $\mathbb{M}_2 \equiv SE(2)$ in Section 6. Again we presented data-driven versions by presenting an exponential curve fit theory in Section 6 that we employed for biomarkers for diabetes in retinal imaging in Section 7.2, and for improved data-driven crossing preserving denoising PDEs in Section 7.3.

Summarizing: we conclude from Theorem 1 and the experiments in Section 7 that the Lie-Cartan connection for $\nu = 1$ is the best choice for geometric multi-orientation image processing, both for crossing-preserving geodesic tracking and for crossing-preserving denoising.

Acknowledgements

Etienne St-Onge and Maxime Descoteaux (Sherbrook Connectivity Imaging Lab, Canada) are gratefully acknowledged for their support in the comparison depicted in Fig. 17. This DW-MRI application is only briefly highlighted in this theoretical overview article, and it is worked out much more profoundly in joint papers with part of the authors of the present paper and them, see previous ISMRM conference article by St.-Onge et al. [51], and previous JMIV article by Smets et al. [41].

Former colleague Michiel Janssen (TU/e, Netherlands) and Javier Olivan Bescos (Philips, Netherlands) are gratefully acknowledged for implementing and visualizing data-driven crossing-preserving diffusions on 3D X-ray data shown in Fig. 18. This 3D X-ray application and the underlying invertible orientation theory is only briefly highlighted in this theoretical overview article, and it is worked out much more profoundly in a JMIV article by Michiel Janssen et al. [45].

The research leading to the results of this article has received funding from the European Research Council under the European Community's 7th Framework Programme (FP7/20072014)/ERC grant agreement No. 335555 (Lie Analysis).

Appendix A. Hamiltonian Flow of the left-invariant (sub)Riemannian Geodesic Problem on Lie group G

The family of all geodesics $\gamma(t)$ augmented to $\mathbf{v}(t) = (\gamma(t), \lambda(t))$ with their momentum representation $\lambda(t) = \sum_{i=1}^{n} \lambda_i(t)\, \omega^i\big|_{\gamma(t)}$ along the geodesic are flow lines of a so-called 'Hamiltonian flow' on the cotangent bundle $T^*(G)$. Controlling the Hamiltonian flow means controlling the complete family of all geodesics (minimal distance curves) together. Next we explain the concept of Hamiltonian flows, and derive the canonical Hamiltonian equations associated to the left-invariant Riemannian and sub-Riemannian problem of interest.

To a Hamiltonian function $\mathfrak{h}$

$$T^*(G) \ni (g, \lambda) \mapsto \mathfrak{h}(g, \lambda) \in \mathbb{R}^+$$

one associates a Hamiltonian vector field $\overrightarrow{\mathfrak{h}}$ (or 'Hamiltonian lift') in the co-tangent bundle. It is determined via the fundamental symplectic form that is given by

$$\sigma = \sum_{i=1}^{n} \omega^i \wedge \text{đ}\lambda_i,$$

where $\text{đ}\lambda_i$ is defined by $\langle \text{đ}\lambda_i, \partial_{\lambda_j} \rangle = \delta^i_j$, by means of

$$\forall_{V=(\dot{g},\dot{\lambda}) \in T_g(G) \times T(T^*_g(G))} \;:\; \sigma(\overrightarrow{\mathfrak{h}}(g, \lambda), V) = \langle \mathrm{d}\mathfrak{h}(g, \lambda), V \rangle. \tag{60}$$

Remark 15 (background on Hamiltonian lifts)
A direct consequence of (60) is that along the flowlines of the Hamiltonian flow the Hamiltonian is preserved (take $V = \overrightarrow{\mathfrak{h}}$) and

$$\frac{d}{dt}\mathfrak{h}(\mathbf{v}(t)) = \sigma(\overrightarrow{\mathfrak{h}}(\mathbf{v}(t)), \overrightarrow{\mathfrak{h}}(\mathbf{v}(t))) = 0, \text{ with } \mathbf{v}(t) = (\gamma(t), \lambda(t)),$$

Furthermore the lifting of a Hamiltionian $\mathfrak{h}$ to its Hamiltonian lift $\overrightarrow{\mathfrak{h}}$ is a Lie algebra isomorphism [62]:

$$\overrightarrow{\{h_1, h_2\}} = [\overrightarrow{h}_1, \overrightarrow{h}_2] \tag{61}$$

where $\{\cdot, \cdot\}$ denote Poisson brackets and $[\cdot, \cdot]$ denotes the usual Lie bracket of vector fields. In the left-invariant (co)-frames Poisson brackets are expressed as

$$\{g, f\} = \sum_{i=1}^{n} (\mathcal{A}_i f)\, \frac{\partial g}{\partial \lambda_i} - \frac{\partial f}{\partial \lambda_i}\, (\mathcal{A}_i g), \tag{62}$$

but this may also be expressed in canonical coordinates [62, eq.11.21].

Remark 16 (simple example of Hamiltonian lifts on $T^*(\mathbb{R})$)
We set $\sigma = \mathrm{d}x \wedge \mathrm{d}\lambda$. We set $\overrightarrow{\mathfrak{h}} = h^1\partial_x + h^2\partial_\lambda$. Then from (60) one can deduce the following standard canonical equations:

$$\overrightarrow{\mathfrak{h}} = \frac{\partial \mathfrak{h}}{\partial \lambda}\partial_x - \frac{\partial \mathfrak{h}}{\partial x}\partial_\lambda + \Rightarrow \dot{x}\partial_x + \dot{\lambda}\partial_\lambda = \dot{\mathbf{v}} = \overrightarrow{\mathfrak{h}}(\mathbf{v}) \Leftrightarrow \begin{cases} \dot{x} = \frac{\partial \mathfrak{h}}{\partial \lambda} \text{ (horizontal part)}, \\ \dot{\lambda} = -\frac{\partial \mathfrak{h}}{\partial x} \text{ (vertical part)}. \end{cases}$$

Generalizing the above example, the next theorem provides the Hamiltonian flows for the left-invariant Riemannian and sub-Riemannian problem on G.

Theorem 2 *The Hamiltonian on Riemannian manifold* $(G, \mathcal{G})$*, with left-invariant metric tensor field* $\mathcal{G}$ *given by (26), equals*

$$\mathfrak{h} = \frac{1}{2}\sum_{i=1}^{n} \lambda^i \lambda_i = \frac{1}{2}\sum_{i,j=1}^{n} g^{ij}\lambda_i\lambda_j \tag{63}$$

and the corresponding Hamiltonian flow (generated by the Hamiltonian vector field $\overrightarrow{\mathfrak{h}}$*) can be written as (recall the definition of linear map* $\tilde{\mathcal{G}}$ *(27))*

$$\begin{aligned} \dot{\mathbf{v}} = \overrightarrow{\mathfrak{h}}(\mathbf{v}) &\Leftrightarrow \begin{cases} \tilde{\mathcal{G}}^{-1}\lambda = \dot{\gamma} \quad \textit{(horizontal part)} \\ \nabla^{[1],*}_{\dot{\gamma}}\lambda = 0 \ \textit{(vertical part)} \end{cases} \\ &\Leftrightarrow \begin{cases} \dot{\gamma}^i = u^i = \lambda^i := \sum\limits_{j=1}^{n} g^{ij}\lambda_j \qquad \textit{(horizontal part)} \\ \dot{\lambda}_i = \{\mathfrak{h}, \lambda_i\} = -\sum\limits_{j,k=1}^{n} c^k_{ij}\lambda_k u^j \ \textit{(vertical part)} \end{cases} \end{aligned} \tag{64}$$

with velocity controls $u^i := \dot{\gamma}^i = \langle \omega^i\big|_{\gamma(\cdot)}, \dot{\gamma}\rangle$ *and* $\mathbf{v}(t) = (\gamma(t), \lambda(t))$ *a curve in the co-tangent bundle* $T^*(G)$ *where the geodesic* $\gamma(t) \in G$ *and the momentum along the geodesic* $\lambda(t) \in T^*_{\gamma(t)}(G)$*, and with* $\{\cdot,\cdot\}$ *denoting Poisson brackets, recall (62).*

The Hamiltonian on sub-Riemannian manifold $(G, \Delta = \mathit{span}\{\mathcal{A}_j\}_{j\in I}, \mathcal{G}_0)$ *equals*

$$\mathfrak{h} = \frac{1}{2}\sum_{i\in I} \lambda^i \lambda_i = \frac{1}{2}\sum_{i,j\in I} g^{ij}\lambda_j\lambda_i \tag{65}$$

and the Hamiltonian flow can be written as

$$\begin{aligned} &\dot{\mathbf{v}} = \overrightarrow{\mathfrak{h}}(\mathbf{v}) \Leftrightarrow \begin{cases} \tilde{\mathcal{G}}_0^{-1}P_{\Delta^*}\lambda = \dot{\gamma} \ \textit{(horizontal part)} \\ \overline{\nabla}^{[1],*}_{\dot{\gamma}}\lambda = 0 \quad \textit{(vertical part)} \end{cases} \Leftrightarrow \\ &\begin{cases} \dot{\gamma}^i = u^i = \lambda^i \textit{ for } i \in I \textit{ and } u^j = 0 \textit{ if } j \notin I \textit{ (horizontal part)} \\ \dot{\lambda}_i = \{\mathfrak{h}, \lambda_i\} = -\sum\limits_{k=1}^{n}\sum\limits_{j\in I} c^k_{ij}\lambda_k u^j \qquad \textit{(vertical part)} \end{cases} \end{aligned} \tag{66}$$

where P_{Δ^*} denotes the projection onto the dual Δ^* of Δ, as given in Theorem 1.

Proof The results (64) and (66) follow from standard application of the Pontryagin Maximum Principle (PMP [62]) to respectively the Riemannian and sub-Riemannian geodesic problem. First of all we note that regarding the Hamiltonian in the Riemannian case (63) we have that it is computed by applying the Fenchel transform on the integrand of the action functional (i.e. squared Lagrangian)

$$\begin{array}{l} \mathfrak{h}(g,\lambda) = \sup\limits_{\dot{\gamma}\in T_g(G)} \{\langle \lambda, \dot{\gamma}\rangle - \mathcal{L}^2(g,\dot{\gamma})\} \text{ with } \lambda = \sum\limits_{i=1}^{n} \lambda_i \; \omega^i\big|_g \in T_g^*(G), \\ \qquad \text{hence we get the Hamiltonian } \mathfrak{h} : T^*(G) \to \mathbb{R}^+ \text{ given by} \\ \qquad \mathfrak{h} = \max\limits_{(v^1,\ldots,v^n)} \left\{ \sum\limits_{i=1}^{n} \lambda_i v^i - \frac{1}{2} \sum\limits_{i,j=1}^{n} v^i v^j g_{ij} \right\} = \frac{1}{2} \sum\limits_{i,j=1}^{n} \lambda^i g_{ij} \lambda^j = \frac{1}{2} \sum\limits_{i=1}^{n} \lambda^i \lambda_i, \end{array} \tag{67}$$

with $\lambda^i = \sum\limits_{j=1}^{n} g^{ij}\lambda_j$. The Hamiltonian in the SR-case (65) comes with the constraint $\dot{\gamma} \in \Delta$ (i.e. $\dot{\gamma}^i = 0$ if $i \notin I$) and then with a similar type of reasoning above (but then with $v^i = 0$ if $i \notin I$) we get $\mathfrak{h} = \frac{1}{2} \sum\limits_{i\in I} \lambda^i \lambda_i$ with $\lambda^i = \sum\limits_{j\in I} g^{ij}\lambda_j$, and we find the 'extremal controls' [62]: $v^i_{max} = u^i = \lambda^i$.

Note that (64) and (66) are of the form $a \Leftrightarrow b \Leftrightarrow c$. We first comment on $a \Leftrightarrow c$ and then show $b \Leftrightarrow c$.

$a \Leftrightarrow c$ follows by direct computation as we show next. By computing We have the following relation in Poisson brackets:

$$[\mathcal{A}_i, \mathcal{A}_j] = \sum_{k=1}^{n} c^k_{ij} \mathcal{A}_k \Leftrightarrow \{\lambda_i, \lambda_j\} = \mathcal{A}_i \lambda_j - \mathcal{A}_j \lambda_i = \sum_{k=1}^{n} c^k_{ij} \lambda_k,$$

as the 'conjugate momentum mapping' gives rise to a Lie-algebra morphism, see [62, p.164]. Thereby (via (62), (67)) we find (with Liouville's theorem and $c^k_{ij} = -c^k_{ji}$):

$$\begin{aligned} \ddot{\gamma}^i &= \dot{u}^i = \{\mathfrak{h}, u^i\} = \dot{\lambda}^i \Rightarrow u^i = \lambda^i, \\ \dot{\lambda}_i &= \{\mathfrak{h}, \lambda_i\} = \sum_{j\in J} \tfrac{2}{2} \{\lambda_j, \lambda_i\} \lambda^j = -\sum_{k=1}^{n} \sum_{j\in J} c^k_{ij} \lambda_k u^j, \end{aligned} \tag{68}$$

which hold for $i = 1, \ldots, n$ in the Riemannian case and for $i \in I$ in the sub-Riemannian case. In the above expression one must set $J = \{1, \ldots, n\}$ in the Riemannian case, and $J = I$ in the sub-Riemannian case.

$b \Leftrightarrow c$ follows by (68), and the expression (25) for the Lie-Cartan connection (with $\nu = 1$), respectively expression (32) for the partial Lie-Cartan connection (again with $\nu = 1$) expressed in left-invariant coordinates. □

Appendix B. Left-Invariant Vector fields on SE(3) via 2 Charts

We need two charts to cover $SO(3)$. When using the following coordinates (ZYZ-Euler angles) for $SE(3) = \mathbb{R}^3 \rtimes SO(3)$ for the first chart:

$$g = (x, y, z, \mathbf{R}_{\mathbf{e}_z,\gamma}\mathbf{R}_{\mathbf{e}_y,\beta}\mathbf{R}_{\mathbf{e}_z,\alpha}), \text{ with } \beta \in (0,\pi), \alpha, \gamma \in [0, 2\pi), \tag{69}$$

Then the left-invariant vector fields are given by:

$$\begin{aligned}
\mathcal{A}_1|_g &= (\cos\alpha\cos\beta\cos\gamma - \sin\alpha\sin\gamma)\partial_x + (\sin\alpha\cos\gamma + \cos\alpha\cos\beta\sin\gamma)\partial_y - \cos\alpha\sin\beta\,\partial_z \\
\mathcal{A}_2|_g &= (-\sin\alpha\cos\beta\cos\gamma - \cos\alpha\sin\gamma)\partial_x + (\cos\alpha\cos\gamma - \sin\alpha\cos\beta\sin\gamma)\partial_y + \sin\alpha\sin\beta\,\partial_z \\
\mathcal{A}_3|_g &= \sin\beta\cos\gamma\,\partial_x + \sin\beta\sin\gamma\,\partial_y + \cos\beta\,\partial_z, \\
\mathcal{A}_4|_g &= \cos\alpha\cot\beta\,\partial_\alpha + \sin\alpha\,\partial_\beta - \tfrac{\cos\alpha}{\sin\beta}\,\partial_\gamma, \mathcal{A}_5|_g = -\sin\alpha\cot\beta\,\partial_\alpha + \cos\alpha\,\partial_\beta + \tfrac{\sin\alpha}{\sin\beta}\,\partial_\gamma, \\
\mathcal{A}_6|_g &= \partial_\alpha.
\end{aligned} \tag{70}$$

The above formula's do not hold for $\beta = \pi$ or $\beta = 0$: We need a second chart [12]:

$$g = (x, y, z, \mathbf{R}_{\mathbf{e}_x,\tilde{\gamma}}\mathbf{R}_{\mathbf{e}_y,\tilde{\beta}}\mathbf{R}_{\mathbf{e}_z,\alpha}), \text{ with } \tilde{\beta} \in [-\pi, \pi), \alpha \in [0, 2\pi), \ \tilde{\gamma} \in (-\frac{\pi}{2}, \frac{\pi}{2}), \tag{71}$$

Then the left-invariant vector field formulas are (for $|\tilde{\beta}| \neq \frac{\pi}{2}$) given by:

$$\begin{aligned}
\mathcal{A}_1|_g &= \cos\alpha\cos\tilde{\beta}\,\partial_x + (\cos\tilde{\gamma}\sin\alpha + \cos\alpha\sin\tilde{\beta}\sin\tilde{\gamma})\,\partial_y + (\sin\alpha\sin\tilde{\gamma} - \cos\alpha\sin\tilde{\beta}\cos\tilde{\gamma})\,\partial_z \\
\mathcal{A}_2|_g &= -\sin\alpha\cos\tilde{\beta}\,\partial_x + (\cos\alpha\cos\tilde{\gamma} - \sin\alpha\sin\tilde{\beta}\sin\tilde{\gamma})\partial_y + (\sin\alpha\sin\tilde{\beta}\cos\tilde{\gamma} + \cos\alpha\sin\tilde{\gamma})\,\partial_z \\
\mathcal{A}_3|_g &= \sin\tilde{\beta}\,\partial_x - \cos\tilde{\beta}\sin\tilde{\gamma}\,\partial_y + \cos\tilde{\beta}\cos\tilde{\gamma}\,\partial_z, \\
\mathcal{A}_4|_g &= -\cos\alpha\tan\tilde{\beta}\,\partial_\alpha + \sin\alpha\,\partial_{\tilde{\beta}} + \tfrac{\cos\alpha}{\cos\tilde{\beta}}\partial_{\tilde{\gamma}}, \mathcal{A}_5|_g = \sin\alpha\tan\tilde{\beta}\,\partial_\alpha + \cos\alpha\partial_{\tilde{\beta}} - \tfrac{\sin\alpha}{\cos\tilde{\beta}}\,\partial_{\tilde{\gamma}}, \\
\mathcal{A}_6|_g &= \partial_\alpha.
\end{aligned} \tag{72}$$

Appendix C. Proofs of Results on Lie-Cartan Connections

Proof of Lemma 2

Let X and Y be vector fields on G and γ the integral curve of X with $\gamma(0) = g$. We write $X = \sum_{i=1}^n x^i \mathcal{A}_i$ and $Y = \sum_{j=1}^n y^j \mathcal{A}_j$. By the definition of $\nabla^{[0]}$ we have that

$$\begin{aligned}
\left(\nabla^{[0]}_{\dot{\gamma}} Y\right)(g) &= \sum_{i,k=1}^n x^i \ \mathcal{A}_i|_g\,(y^k)\ \mathcal{A}_k|_g = \sum_{k=1}^n X|_g\,(y^k)\ \mathcal{A}_k|_g \\
&= \sum_{k=1}^n \left(\lim_{t\to 0} \frac{y^k(\gamma(t)) - y^k(g)}{t}\right) \mathcal{A}_k|_g \\
&= \lim_{t\to 0} \frac{\sum_{k=1}^n y^k(\gamma(t)) \left(L_{g\gamma(t)^{-1}}\right)_* \mathcal{A}_k|_{\gamma(t)} - Y(g)}{t} \\
&= \lim_{t\to 0} \frac{\left(L_{g\gamma(t)^{-1}}\right)_* Y(\gamma(t)) - Y(g)}{t} .
\end{aligned}$$

This proves (14).

Now let X, Y be left-invariant. Note that $\nabla^{[0]}Y = 0$ because $\left(L_{g(\gamma(t))^{-1}*}\right) Y(\gamma(t)) = Y(g)$ in (14) regardless of γ. Then the alternative formula (15) for general Lie-Cartan Connection $\nabla^{[\nu]}$ follows, as the structure constants $c^k_{ij} \in \mathbb{R}$ satisfy $\sum_k c^k_{ij}\mathcal{A}_k = [\mathcal{A}_i, \mathcal{A}_j]$ and the Lie bracket is bilinear for left-invariant vector fields, and we find $\nabla^{[\nu]}_X Y = \nabla^{[0]}_X Y + \nu[X,Y] \; = \nu[X,Y]$

For our reformulation in (15) we used (17):$(\widetilde{\mathrm{Ad}})_*(X_g)(Y_g) = [X_g, Y_g]$ that we show next. By the derivation in [58, Lemma.5.4.2] one has $(Ad)_*(X_e)(Y_e) = [X_e, Y_e]$. Now the Cartan-Maurer form is a Lie algebra isomorphism, and we get (17):

$$\begin{aligned}\widetilde{\mathrm{Ad}}_*(X_g)(Y_g) &= \widetilde{\mathrm{Ad}}_*((L_g)_*X_e)((L_g)_*Y_e) \overset{(16)}{=} (L_g)_*\mathrm{Ad}_*(X_e, Y_e)\\ &= [(L_g)_*X_e, (L_g)_*Y_e] = [X_g, Y_g].\end{aligned}$$

Proof of Lemma 3

Let X, Y, Z be left-invariant vector fields. For all computations, we use the characterisation of Lie-Cartan connections (15) from Lemma 2.

Torsion of $\nabla^{[\nu]}$: We have

$$\begin{aligned}T_{\nabla^{[\nu]}}(X,Y) &= \nabla^{[\nu]}_X Y - \nabla^{[\nu]}_Y X - [X,Y]\\ &= \nu[X,Y] - \nu[Y,X] - [X,Y] = (2\nu - 1)[X,Y].\end{aligned}$$

Curvature of $\nabla^{[\nu]}$: By the Jacobi identity for Lie brackets we have

$$\begin{aligned}R_{\nabla^{[\nu]}}(X,Y)Z &= \nabla^{[\nu]}_X\nabla^{[\nu]}_Y Z - \nabla^{[\nu]}_Y\nabla^{[\nu]}_X Z - \nabla^{[\nu]}_{[X,Y]} Z\\ &= \nu^2\left([X,[Y,Z]] - [Y,[X,Z]]\right) - \nu\,[[X,Y],Z]\\ &= \nu^2\,[[X,Y],Z] - \nu\,[[X,Y],Z] = \nu(\nu-1)[[X,Y],Z]\end{aligned}$$

Metric compatibility: We have

$$\begin{aligned}\nabla^{[\nu]}\mathcal{G}(X,Y,Z) &= X(\mathcal{G}(Y,Z)) - \mathcal{G}\left(Y, \nabla^{[\nu]}_X Z\right) - \mathcal{G}\left(\nabla^{[\nu]}_X Y, Z\right)\\ &= X(\mathcal{G}(Y,Z)) - \nu\,\mathcal{G}(Y,[X,Z]) - \nu\,\mathcal{G}([X,Y],Z)\\ &= -\nu\left(\mathcal{G}(Y,[X,Z]) + \mathcal{G}([X,Y],Z)\right)\,,\end{aligned}$$

where we note that $X(\mathcal{G}(Y,Z)) = 0$ because $\mathcal{G}$ is also left invariant.

Literature

1. G. Citti and A. Sarti, “A cortical based model of perceptional completion in the roto-translation space,” *Journal of Mathematical Imaging and Vision*, vol. 24, no. 3, pp. 307–326, 2006.

2. E. Baspinar, *Minimal Surfaces in Sub-Riemannian Structures and Functional Geometry of the Visual Cortex*. PhD thesis, University of Bologna, 2018.
3. R. Duits, M. Felsberg, G. Granlund, and B. M. ter Haar Romeny, “Image analysis and reconstruction using a wavelet transform constructed from a reducible representation of the Euclidean motion group,” *International Journal of Computer Vision*, vol. 79, no. 1, pp. 79–102, 2007.
4. E. Bekkers, *Retinal Image Analysis using Sub-Riemannian Geometry in $SE(2)$*. PhD thesis, Eindhoven University of Technology, 2017. cum laude ($\leq$ 5% best at TU/e), URL: *https://pure.tue.nl/ws/files/52750592/20170123 _ Bekkers.pdf*.
5. P.-E. Forssen, *Low and Medium Level Vision using Channel Representations*. PhD thesis, Linkoping University, Sweden, 2004. Dissertation No. 858, ISBN 91-7373-876-X.
6. M. Felsberg, P.-E. Forssen, and H. Scharr, “Channel smoothing: Efficient robust smoothing of low-level signal features,” *IEEE Transactions on Pattern Analysis and Machine Intelligence*, pp. 209–222, 2006.
7. R. Duits and E. M. Franken, “Left invariant parabolic evolution equations on $SE(2)$ and contour enhancement via invertible orientation scores, part I: Linear left-invariant diffusion equations on $SE(2)$,” *Quarterly of Applied mathematics, AMS*, vol. 68, pp. 255–292, June 2010.
8. M. H. J. Janssen, A. J. E. M. Janssen, E. J. Bekkers, J. O. Bescós, and R. Duits, “Design and processing of invertible orientation scores of 3d images,” *Journal of Mathematical Imaging and Vision*, Mar 2018.
9. J. Zhang, R. Duits, B. ter Haar Romeny, and G. Sanguinetti, “Numerical approaches for linear left-invariant diffusions on $SE(2)$, their comparisons to exact solutions, and their applications in retinal imaging,” *Numerical Mathematics: Theory Methods and Applications*, vol. 9, pp. 1–50, January 2016.
10. R. Duits, E. St-Onge, J. Portegies, and B. Smets, “Total variation and mean curvature PDEs on the space of positions and orientations,” in *Scale Space and Variational Methods in Computer Vision - 7th International Conference, SSVM 2019, Proceedings* (J. Lellmann, J. Modersitzki, and M. Burger, eds.), Lecture Notes in Computer Science (including subseries Lecture Notes in Artificial Intelligence and Lecture Notes in Bioinformatics), (Germany), pp. 211–223, Springer, 6 2019.
11. M. Felsberg, *Adaptive Filtering Using Channel Representations*, pp. 31–48. London: Springer London, 2012.
12. R. Duits and E. M. Franken, “Left-invariant diffusions on the space of positions and orientations and their application to crossing-preserving smoothing of HARDI images.,” *International Journal of Computer Vision, IJCV*, vol. 92, pp. 231–264, 2011.
13. G. Citti, B. Franceschiello, G. Sanguinetti, and A. Sarti, “Sub-Riemannian mean curvature flow for image processing,” *SIIMS*, vol. 9, no. 1, pp. 212–237, 2016.
14. P. Momayyez-Siahkal and K. Siddiqi, “3d Stochastic Completion Fields for Fiber Tractography,” in *Proc IEEE Comput Soc Conf Comput Vis Pattern Recognit*, pp. 178–185, June 2009.
15. E. Piuze, J. Sporring, and K. Siddiqi, “Maurer-cartan forms for fields on surfaces: Application to heart fiber geometry,” *IEEE Transactions on Pattern Analysis and Machine Intelligence*, vol. 37, no. 12, pp. 2492–2504, 2015.
16. R. Duits, M. H. Janssen, J. Hannink, and G. R. Sanguinetti, “Locally adaptive frames in the roto-translation group and their applications in medical imaging,” *J. Math. Imaging Vis.*, vol. 56, no. 3, pp. 367–402, 2016.
17. J. Zhang, B. Dashtbozorg, E. Bekkers, J. Pluim, R. Duits, and B. ter Haar Romeny, “Robust retinal vessel segmentation via locally adaptive derivative frames in orientation scores,” *IEEE-TMI*, vol. 35, no. 12, pp. 2631–2644, 2016.
18. E. Bekkers, J. Zhang, R. Duits, and B. ter Haar Romeny, “Curvature based biomarkers for diabetic retinopathy via exponential curve fits in se(2),” in *Proc. of the Ophthalmic Medical Image Analysis Int. Workshop* (X. e. a. Chen, ed.), (October), pp. 113–120, 2015.

19. R. Duits, S. P. L. Meesters, J.-M. Mirebeau, and J. M. Portegies, "Optimal Paths for Variants of the 2d and 3d Reeds-Shepp Car with Applications in Image Analysis," *JMIV*, vol. 60, pp. 816–848, July 2018.
20. V. Prčkovska, M. Andorrà, P. Villoslada, E. Martinez-Heras, R. Duits, D. Fortin, P. Rodrigues, and M. Descoteaux, "Contextual diffusion image post-processing aids clinical applications," in *Visualization and Processing of Higher Order Descriptors for Multi-Valued Data* (I. Hotz and T. Schultz, eds.), (Cham), pp. 353–377, Springer International Publishing, 2015.
21. E. M. Franken, *Enhancement of Crossing Elongated Structures in Images*. PhD thesis, Department of Biomedical Engineering, Eindhoven University of Technology, The Netherlands, Eindhoven, October 2008. cum laude and selected for promotion prize (≤ 2% best at TU/e).
22. J. Petitot, "The neurogeometry of pinwheels as a sub-Riemannian contact structure," *Journal of Physiology - Paris*, vol. 97, pp. 265–309, 2003.
23. W. H. Bosking, Y. Zhang, B. Schofield, and D. Fitzpatrick, "Orientation selectivity and the arrangement of horizontal connections in tree shrew striate cortex," *The Journal of Neuroscience*, vol. 17, pp. 2112–2127, March 1997.
24. A. Chambolle and T. Pock, "Total roto-translation variation," *Arxiv*, pp. 1–47, july 2018.
25. E. M. Franken and R. Duits, "Crossing preserving coherence-enhancing diffusion on invertible orientation scores," *International Journal of Computer Vision (IJCV)*, vol. 85, no. 3, pp. 253–278, 2009.
26. J. M. Portegies, R. H. J. Fick, G. R. Sanguinetti, S. P. L. Meesters, G. Girard, and R. Duits, "Improving Fiber Alignment in HARDI by Combining Contextual PDE Flow with Constrained Spherical Deconvolution," *PLoS ONE*, vol. 10, no. 10, 2015. doi: 10.1371/journal.pone.0138122.
27. S. Meesters, P. Ossenblok, L. Wagner, O. Schijns, P. Boon, L. Florack, Vilanova, and R. Duits, "Stability metrics for optic radiation tractography: Towards damage prediction after resective surgery," *Journal of Neuroscience Methods*, 2017. doi: 10.1016/j.jneumeth.2017.05.029.
28. D. Chen and L. Cohen, "Fast asymmetric fronts propagation for image segmentation," *Journal of Mathematical Imaging and Vision*, vol. 60, pp. 766–783, 2018.
29. M. Janssen, R. Duits, and M. Breeuwer, "Invertible orientation scores of 3D images," in *SSVM-LNCS*, vol. 9087, pp. 563–575, 2014.
30. E. Bekkers, R. Duits, A. Mashatkov, and G. Sanguinetti, "A PDE approach to data-driven sub-Riemannian geodesics in $SE(2)$," *SIAM Journal of Imaging Science*, vol. 8, no. 4, pp. 2740–2770, 2015.
31. R. Duits, M. Janssen, J. Hannink, and G. Sanguinetti, "Locally adaptive frames in the roto-translation group and their applications in medical image processing," *JMIV*, vol. 56, no. 3, pp. 367–402, 2016.
32. B. Smets, J. Portegies, E. Bekkers, and R. Duits, "Pde-based group equivariant convolutional neural networks," tech. rep., Dep. Mathematics and Computer Science TU/e, January 2020. arXiv:.
33. E. Bekkers, M. Lafarge, M. Veta, K. Eppenhof, J. Pluim, and R. Duits, "Roto-translation covariant convolutional networks for medical image analysis," in *Medical Image Computing and Computer Assisted Intervention – MICCAI 2018* (F. et al., ed.), (Cham), pp. 440–448, Springer International Publishing, 2018.
34. T. Cohen and M. Welling, "Group equivariant convolutional networks," *Proc. of the 33rd Int. Conf. on Machine Learning*, vol. 48, pp. 1–12, 2016.
35. R. Duits, H. Fuehr, B. Janssen, L. Florack, and H. van Assen, "Evolution equations on gabor transforms and their applications," *ACHA*, vol. 35, no. 3, pp. 483–526, 2013.
36. D. Barbieri, G. Citti, G. Cocci, and A. Sarti, "A cortical-inspired geometry for contour perception and motion integration," *Journal of Mathematical Imaging and Vision*, vol. 49, no. 3, pp. 511–529, 2014.
37. A. Mashtakov, R. Duits, Y. Sachkov, E. Bekkers, and I. Beschastnyi, "Tracking of lines in spherical images via sub-Riemannian geodesics in SO(3)," *JMIV*, vol. 58, no. 2, pp. 239–364, 2017.
38. U. Sharma and R. Duits, "Left-invariant evolutions of wavelet transforms on the similitude group," *ACHA*, vol. 39, pp. 110–137, 2015.

39. R. Duits, E. Creusen, A. Ghosh, and T. Dela Haije, "Morphological and linear scale spaces for fiber enhancement in DW-MRI," *Journal of Mathematical Imaging and Vision*, vol. 46, pp. 326–368, July 2013.
40. R. Duits, E. J. Bekkers, and A. Mashtakov, "Fourier transform on the homogeneous space of 3d positions and orientations for exact solutions to linear PDEs," *Entropy: Special Issue: Joseph Fourier 250th Birthday: Modern Fourier Analysis and Fourier Heat Equation in Information Sciences for the XXIst century*, vol. 21, no. 1, pp. 1–38, 2019.
41. B. Smets, R. Duits, E. St-Onge, and J. Portegies, "Total variation and mean curvature PDEs on the homogeneous space of positions and orientations," *Submitted to JMIV special issue*, 2019.
42. R. Duits, *Perceptual Organization in Image Analysis*. PhD thesis, Eindhoven University of Technology, Dep. of Biomedical Engineering, The Netherlands, 2005.
43. S. Ali, J. Antoine, and J. Gazeau, *Coherent States, Wavelets and Their Generalizations*. New York, Berlin, Heidelberg: Springer Verlag, 1999.
44. H. Fuehr, *Abstract Harmonic Analysis of Continuous Wavelet Transforms*. Heidelberg-New York: Springer, 2005.
45. M. H. J. Janssen, A. J. E. M. Janssen, J. Olivan Bescos, and R. Duits, "Design and processing of invertible orientation scores of 3d images," *Journal of Mathematical Imaging and Vision*, vol. 60, no. 9, pp. 1427–1458, 2018.
46. A. Grossmann, J. Morlet, and T. Paul, "Integral transforms associated to square integrable representations," *J.Math.Phys.*, vol. 26, pp. 2473–2479, 1985.
47. J. Dieudonné, *Treatise on Analysis*, vol. V. New York: AP, 1977.
48. E. Bekkers, R. Duits, T. Berendschot, and B. Haar Romeny, "A multi-orientation analysis approach to retinal vessel tracking," *JMIV*, vol. 49, no. 3, pp. 583–610, 2014.
49. R. Duits and E. Bekkers, "Lecture notes of the course "Differential Geometry for Image Processing", Part II: Invertible Orientation Scores," tech. rep., TU/e Dep. of Mathematics and Computer Science, 2020. www.win.tue.nl/~rduits/partIIversion1.pdf.
50. F. Martin and R. Duits, "Lie analysis homepage." url: *http://www.lieanalysis.nl/*, 2017.
51. E. St Onge, S. Meesters, E. Bekkers, M. Descoteaux, and R. Duits, "Hardi denoising with mean-curvature enhancement pde on SE(3)," in *ISMRM Proceedings* (J. et al., ed.), (Montreal, Canada), pp. 1–3, 2019. http://archive.ismrm.org/2019/3409.html.
52. E. Bekkers, R. Duits, A. Mashtakov, and Y. Sachkov, "Vessel tracking via sub-Riemannian geodesics on $\mathbb{R}^2 \rtimes P^1$," *LNCS Proceedings Geometric Science of Information GSI 2017*, vol. 10589, pp. 1611–3349, 2017.
53. S. Kobayashi and K. Nomizu, *Foundations of differential geometry*, vol. 1. New York, 1963.
54. A. Cogliati and P. Mastrolia, "Cartan, schouten and the search for connection," *Historia Mathematica*, vol. 45, no. 1, pp. 39–74, 2018.
55. I. Kolar, J. Slovak, and P. Michor, *Natural operations in differential geometry*. Springer-Verlag, 1999. corrected version of original version in 1993.
56. É. Cartan, "Sur une classe remarquable d'espaces de riemann," *Bulletin de la Société Mathématique de France*, vol. 54, pp. 214–264, 1926.
57. J. M. Lee, B. Chow, S.-C. Chu, D. Glickenstein, C. Guenther, J. Isenberg, T. Ivey, D. Knopf, P. Lu, F. Luo, *et al.*, "Manifolds and differential geometry," *Topology*, vol. 643, p. 658, 2009.
58. J. Jost, *Riemannian Geometry and Geometric Analysis*. Springer-Verlag, 2011.
59. G. S. Chirikjian and A. B. Kyatkin, *Engineering applications of noncommutitative harmonic analysis: with emphasis on rotation and motion groups*. Boca Raton CRC Press, 2001.
60. A. Saccon, A. P. Aguiar, A. J. Hausler, J. Hauser, and A. M. Pascoal, "Constrained motion planning for multiple vehicles on se(3)," in *2012 IEEE 51st IEEE Conference on Decision and Control (CDC)*, pp. 5637–5642, Dec 2012.
61. G. Citti and A. Sarti, *Models of the Visual Cortex in Lie Groups*, pp. 1–55. Basel: Springer Basel, 2015.
62. A. A. Agrachev and Y. L. Sachkov, *Control Theory from the Geometrical Viewpoint*, vol. 87. Springer-Verlag, 2004.
63. L. Hormander, "Hypoellptic second order differential equations," *Acta Mathematica*, vol. 119, pp. 147–171, 1968.

64. A. Agrachev, D. Barilari, and U. Boscain, *A Comprehensive Introduction to Sub-Riemannian Geometry*. CUP Cambridge studies in advanced mathematics, 2020.
65. Y. Sachkov, "Cut locus and optimal synthesis in the sub-Riemannian problem on the group of motions of a plane," *ESAIM: Control, Optimization and Calculus of Variations*, vol. 17, pp. 293–321, 2011.
66. Y. Sachkov, "Maxwell strata in the euler elastic problem," *Journal of Dynamical and Control Systems*, vol. 14, no. 2, pp. 169–234, 2008.
67. R. Bryant and P. Griffiths, "Reduction for constrained variational problems and $(1/2)\int \kappa^2 \mathrm{ds}$," *American Journal of Mathematics*, vol. 108, no. 3, pp. 525–570, 1986.
68. D. Mumford, "Elastica and computer vision," *Algebraic Geometry and Its Applications. Springer-Verlag*, pp. 491–506, 1994.
69. J. Petitot, *Elements of Neurogeometry*. Lecture Notes in Morphogenesis, Springer, 2017.
70. R. Duits, A. Ghosh, T. Dela Haije, and A. Mashtakov, "On sub-Riemannian geodesics in $SE(3)$ whose spatial projections do not have cusps," *Journal of Dynamical Control Systems*, vol. 22, no. 4, pp. 771–805, 2016.
71. R. Bryant, P. Griffiths, and D. Grossman, *Exterior Differential Systems and Euler-Lagrange Partial Differential Equations*. Chicago and London: Chicago Lectures in Mathematics, 2003.
72. M. Crandall and P.-L. Lions, "Viscosity solutions of hamilton-jacobi equations," *Trans. A.M.S.*, vol. 277, no. 1, pp. 1–42, 1983.
73. L. C. Evans, *Partial differential equations*. Providence, R.I.: American Mathematical Society, 2010.
74. C. Mantegazza and A. Mennucci, "Hamilton-jacobi equations and distance functions on Riemannian manifolds," *App. Math. and Optim.*, vol. 47, no. 1, pp. 1–25, 2002.
75. R. Monti and F. Cassano, "Surface measures in Carnot-carathéody spaces," *Calc. Var.*, vol. 13, pp. 339–376, 2001.
76. R. Duits and E. M. Franken, "Left invariant parabolic evolution equations on $SE(2)$ and contour enhancement via invertible orientation scores, part II: Nonlinear left-invariant diffusion equations on invertible orientation scores," *Quarterly of Applied mathematics, AMS*, vol. 68, pp. 293–331, June 2010.
77. R. Duits, M. Felsberg, G. Granlund, and B. M. t. Haar Romeny, "Image analysis and reconstruction using a wavelet transform constructed from a reducible representation of the Euclidean motion group," *International Journal of Computer Vision*, vol. 72, pp. 79–102, April 2007.
78. J. Mirebeau, "Fast marching methods for curvature penalized shortest paths," *to appear in JMIV: SI: Orientation Analysis and Differential Geometry in Image Processing*, 2018.
79. G. Sanguinetti, E. Bekkers, R. Duits, M. H. J. Janssen, A. Mashtakov, and J.-M. Mirebeau, *Sub-Riemannian Fast Marching in SE(2)*. Springer, 2015.
80. J. Mirebeau, "Anisotropic Fast-Marching on Cartesian Grids Using Lattice Basis Reduction," *SIAM J. Numer. Anal.*, vol. 52, no. 4, pp. 1573–1599, 2014.
81. J. Mirebeau and J. Portegies, "Hamiltonian fast marching: A numerical solver for anisotropic and non-holonomic eikonal PDEs," *IPOL*, pp. 47–93, 2019.
82. E. Bekkers, M. Loog, B. ter Haar Romeny, and R. Duits, "Template matching via densities on the roto-translation group," *IEEE Transactions on Pattern Analysis and Machine Intelligence*, vol. 40, pp. 452–466, Februari 2018.
83. B. Smets, "Geometric image denoising and machine learning (cum laude)," Master's thesis, Industrial and Applied Mathematics, CASA-TU/e, June 2019. Supervisor R.Duits, url: *www.win.tue.nl/ rduits/reportBartSmets.pdf*.
84. M. Janssen, T. Dela Haije, F. Martin, E. Bekkers, and R. Duits, "The hessian of axially symmetric functions on $se(3)$ and application in 3d image analysis," *LNCS*, vol. –, pp. –, 2017. Submitted to SSVM 2017.
85. E. M. Franken and R. Duits, "Crossing-preserving coherence-enhancing diffusion on invertible orientation scores," *International Journal of Computer Vision (IJCV)*, vol. 85, no. 3, pp. 253–278, 2009.

86. B. Haar Romenij, ter, *Front-end vision and multi-scale image analysis : multi-scale computer vision theory and applications, written in Mathematica*. Computational imaging and vision. CIVI, Netherlands: Kluwer Academic Publishers, 2003.
87. M. Bertalmío, L. Calatroni, V. Franceschi, B. Franceschiello, and D. Prandi, "A cortical-inspired model for orientation-dependent contrast perception: A link with wilson-cowan equations," in *Scale Space and Variational Methods in Computer Vision* (J. Lellmann, M. Burger, and J. Modersitzki, eds.), (Cham), pp. 472–484, Springer International Publishing, 2019.
88. L. Siffre, *Rigid-Motion Scattering for Image Classification*. PhD thesis, Ecole Polytechnique, Paris, 2014.
89. J. Hannink, R. Duits, and E. Bekkers, "Crossing-preserving multi-scale vesselness," in *MICCAI* (G. et al., ed.), vol. 8674, pp. 603–610, 2014.
90. A. Frangi et al., "Multiscale vessel enhancement filtering," *Proceedings of Medical Image Computing and Computer-Assisted Intervention: Lecture Notes in Computer Science*, vol. 1496, pp. 130–137, 1998.
91. D. Chen, *New Minimal Paths Models for Tubular Structure Extraction and Image Segmentation*. PhD thesis, Université Paris Dauphine, PSL Research University, 2016.
92. B. Franceschiello, A. Mashtakov, G. Citti, and A. Sarti, "Geometrical optical illusion via sub-riemannian geodesics in the roto-translation group," *Differential Geometry and its Applications*, vol. 65, pp. 55 – 77, 2019.
93. E. Creusen, R. Duits, and T. Dela Haije, "Numerical schemes for linear and non-linear enhancement of dw-mri," in *International Conference on Scale Space and Variational Methods in Computer Vision*, pp. 14–25, Springer, Berlin, Heidelberg, 2011.
94. M. Reisert and V. G. Kiselev, "Fiber Continuity: An Anisotropic Prior for ODF Estimation.," *IEEE Transactions on Medical Imaging*, vol. 30, no. 6, pp. 1274–1283, 2011.
95. H. Skibbe and M. Reisert, "Spherical tensor algebra: A toolkit for 3d image processing," *JMIV*, vol. 58, pp. 349–381, 2017.
96. E. J. Bekkers, D. Chen, and J. M. Portegies, "Nilpotent Approximations of Sub-Riemannian Distances for Fast Perceptual Grouping of Blood Vessels in 2d and 3d," *arXiv:1707.02811 [math]*, July 2017. arXiv: 1707.02811.
97. J. Portegies, G. Sanguinetti, S. Meesters, and R. Duits, "New approximation of a scale space kernel on SE(3) and applications in neuroimaging," in *SSVM 2015, LNCS 9087*, pp. 40–52, 2015.
98. J.-M. Mirebeau, "Fast marching methods for curvature penalized shortest paths," *Journal of Mathematical Imaging and Vision, Special Issue: Orientation Analysis and Differential Geometry in Image Processing*, vol. 60, no. 6, pp. 784–815, 2018.
99. J. Portegies, *PDEs on the Lie Group SE(3) and their Applications in Diffusion-Weighted MRI*. PhD thesis, Department of Mathematics and Computer Science, TU/e, February 2018.
100. J. Portegies, S. Meesters, P. Ossenblo, A. Fuster, L. Florack, and R. Duits, *Brain Connectivity Measures via Direct Sub-Finslerian Front Propagation on the 5D Sphere Bundle of Positions and Directions*, ch. 24, p. 14. Springer, 2019.
101. M. Pechaud, M. Descoteaux, and R. Keriven, *Brain Connectivity Using Geodesics in HARDI*, pp. 482–489. Berlin, Heidelberg: Springer Berlin Heidelberg, 2009.
102. V. Caselles, R. Kimmel, and G. Sapiro, "Geodesic active contours," *International journal of computer vision*, vol. 22, no. 1, pp. 61–79, 1997.
103. A. F. M. ter Elst and D. W. Robinson, "Weighted subcoercive operators on Lie groups," *Journal of Functional Analysis*, vol. 157, pp. 88–163, 1998.
104. J. Zhang, B. Dashtbozorg, F. Huang, T. T. Berendschot, and B. M. ter Haar Romeny, "Analysis of retinal vascular biomarkers for early detection of diabetes," in *European Congress on Computational Methods in Applied Sciences and Engineering*, pp. 811–817, Springer, 2017.
105. S. Zhu *et al.*, "Retinal vascular tortuosity in hospitalized patients with type 2 diabetes and diabetic retinopathy in china," *Journal of Biomedical Science and Engineering*, vol. 9, no. 10, p. 143, 2016.
106. S. Zhu, H. Liu, R. Du, D. S. Annick, S. Chen, and W. Qian, "Tortuosity of retinal main and branching arterioles, venules in patients with type 2 diabetes and diabetic retinopathy in china," *IEEE Access*, vol. 8, pp. 6201–6208, 2020.

107. E. M. Franken, R. Duits, and B. M. ter Haar Romeny, "Curvature estimation for enhancement of crossing curves," in *Digital Proceedings of the 8th IEEE Computer Society Workshop on Mathematical Methods in Biomedical Image Analysis (MMBIA), held in conjuction with the IEEE International Conference on Computer Vision (Rio de Janeiro, Brazil)* (Niessen, Westin, and Nielsen, eds.), pp. 1–8, Omnipress, October 2007. Awarded the *MMBIA 2007 best paper award*.
108. M. Lebrun, "An analysis and implementation of the bm3d image denoising method," *IEEE Trans. Image Processing*, vol. 2, pp. 175–213, 2012.
109. K. Dabov, A. Foi, V. Katkovnik, and K. Egiazarian, "Image denoising by sparse 3d transform-domain collaborative filtering," *IEEE Trans. Image Processing*, vol. 16, no. 8, pp. 2080–2095, 2007.
110. U. Boscain, R. Chertovskih, J.-P. Gauthier, D. Prandi, and A. Remizov, "Cortical-inspired image reconstruction via sub-Riemannian geometry and hypoelliptic diffusion." arXiv:1801.03800, 2018.
111. A. Chambolle and T. Pock, "A first-order primal-dual algorithm for convex problems with applications to imaging," *Journal of Mathematical Imaging and Vision*, vol. 40, no. 1, pp. 120–145, 2011.
112. P. Perona and J. Malik, "Scale-space and edge detection using anisotropic diffusion," *IEEE Trans. Pattern Anal. Mach. Intell.*, vol. 12, no. 7, 1990.
113. J. Weickert, "Coherence-enhancing diffusion filtering.," *International Journal of Computer Vision*, vol. 31, no. 2/3, pp. 111–127, 1999.
114. L. Fabbrini, M. Greco, M. Messina, and G. Pinelli, "Improved edge enhancing diffusion filter for speckle-corrupted images," *IEEE Geoscience and Remote Sensing Letters*, vol. 11, no. 1, pp. 99–103, 2013.
115. E. Creusen, R. Duits, A. Vilanova, and L. Florack, "Numerical schemes for linear and non-linear enhancement of dw-mri," *Numerical Mathematics: Theory, Methods and Applications*, vol. 6, no. 1, pp. 138–168, 2013.
116. J. D. Tournier, F. Calamante, and A. Connelly, "Robust determination of the fibre orientation distribution in diffusion mri: non-negativity constrained super-resolved spherical deconvolution.," *Neuroimage*, vol. 35, no. 4, pp. 1459–1472, 2007.
117. M. Descoteaux, R. Deriche, T. R. Knosche, and A. Anwander, "Deterministic and probabilistic tractography based on complex fibre orientation distributions.," *IEEE transactions on medical imaging*, vol. 28, no. 2, pp. 269–286, 2009.